CHALMERS
UNIVERSITY OF TECHNOLOGY

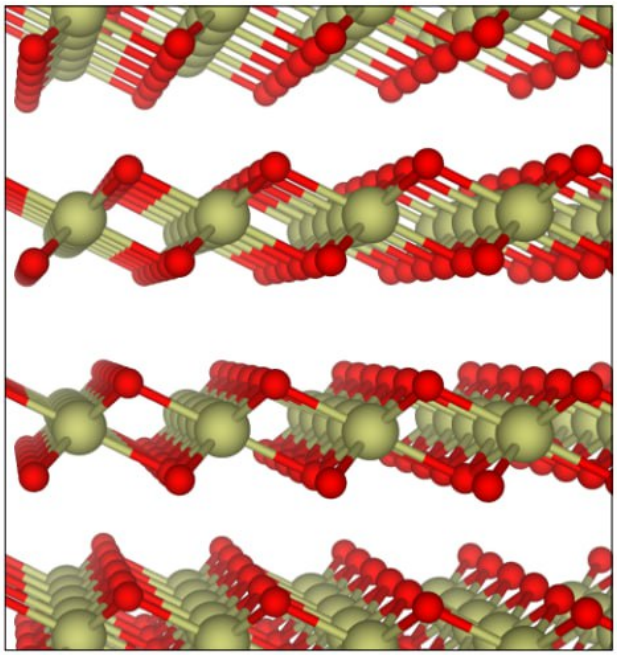

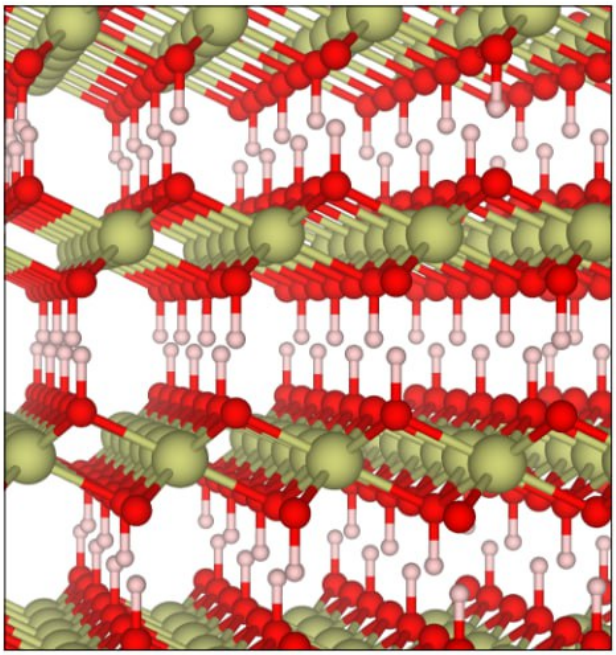

Computational Modeling of Layered Structures of IrO_2 and IrOOH

Master's thesis in Condensed Matter and Materials theory

Saraswat Nikhil

DEPARTMENT OF PHYSICS

CHALMERS UNIVERSITY OF TECHNOLOGY
Gothenburg, Sweden 2024
www.chalmers.se

CHALMERS UNIVERSITY OF TECHNOLOGY

TIFX05 Master Thesis in Physics

Computational Modeling of Layered Structure of IrO_2 and IrOOH

Author: Nikhil Saraswat

Supervisor : Mehmet Baskurt

Examiner : Dr Julia Wiktor

Date: 24 October 2024

CHALMERS
UNIVERSITY OF TECHNOLOGY

Department of Physics
Division of Condensed Matter and Materials Theory
Chalmers University of Technology
Gothenburg, Sweden 2024

Computational Modeling of Layered Structure of IrO_2 and IrOOH
Saraswat Nikhil

Supervisor: Mehmet Baskurt, Department Physics
Examiner: Dr Julia Wiktor, Department Physics

Master's Thesis 2024
Department of Physics
Division of Condensed Matter and Materials Theory

Chalmers University of Technology
SE-412 96 Gothenburg
Telephone +46 31 772 3257

Cover: Crystal structure of layered IrO_2 and IrOOH

Typeset in LaTeX
Printed by Chalmers Reproservice
Gothenburg, Sweden 2024

Abstract

The increasing demand for clean energy has intensified research into materials that can enhance the efficiency of electrochemical processes such as water electrolysis. Layered transition metals oxides and oxyhydroxides have drawn interest because of their versatility as an electrocatalyst. Iridium-based catalysts have gained particular interest for their multivalent state among these electrocatalysts. Here, we examine the electronic and structural characteristics of layered IrO_2 and IrOOH. This thesis presents a comprehensive computational study of the structural, electronic, and vibrational properties of IrO_2 and IrOOH, using Density Functional Theory (DFT) with van der Waals (vdW) corrections to investigate and model the structures. Using functionals such as PBE+rVV10L and SCAN+rVV10, various stacking arrangements (AA, AB, AA′, and AB′) for IrO_2 were investigated, with AA stacking consistently predicted as the lowest energetically configuration. The minimal energy differences between AA and AB′ stackings suggest the potential for stacking faults. Additionally, the impact of structural distortions on the dynamical stability and electronic properties of IrO_2 was explored, revealing that distortions can induce a transition from metallic to semiconducting behavior. IrOOH is modeled by hydrogenating the IrO_2 structure, and both pristine and distorted configurations were analyzed. The electronic band structure predicts that IrOOH behaves as a semiconductor, where the distorted structure reverts to pristine-like. This work deepens our understanding of the structural and electronic properties that contribute to modeling the layered structures of IrO_2 and IrOOH. Such insights are expected to be crucial for future theoretical and experimental efforts to optimize the materials for green energy technologies, including water splitting and other electrochemical applications.

Keywords: Layered material, transition metals, oxides, hydroxides, IrO_2, IrOOH, density functional theory, Dynamic stability,

Acknowledgements

My sincere gratitude goes to Julia Wiktor, my examiner, for her constant support, encouragement, guidance, and patience with my questions during this thesis. I am grateful that you offered me the opportunity to work on this thesis and provided me with a platform to learn and grow.

A very special thanks to my supervisor Mehmet Baskurt. Thank you for your time and effort to make this thesis a reality. You have been patient, understanding, and helpful throughout the thesis. I wish you the best for all your future endeavors.

I express my sincere gratitude to Chalmers University and the Department of Physics, especially the Condensed Matter and Material Theroy Division, for providing the tools and setting I needed to complete my thesis successfully. Your help has been valuable, and I am grateful for all the support I have had.

Thanks to the department for their helpful input, fun interactions, and the lovely fika breaks. I am also grateful to my friends who helped me with their valuable insights and suggestions.

Last but not least, I would like to extend my gratitude to all of my friends and family who have helped me get to this point.

Saraswat Nikhil, Göteborg, October 2024

Contents

List of Figures

1

Introduction

Since the beginning of the industrial revolution, new inventions and technologies have been continuously making human life more convenient. The world has grown dependent on the excessive usage of non-renewable energy resources such as coal, natural gas, and petroleum to sustain human activities. With the global population rising, energy demand continues to increase, and it is predicted to double in the next 15 years. This raises energy and environmental concerns, motivating many researchers to develop green and sustainable energy systems for long-term development. The promising idea is to store renewable energy in the form of fuels and produce high-value chemicals to drive the goal of attaining clean and green energy through energy conversion or storage systems [1, 2, 3, 4]. Among the variety of energy conversion processes, water electrolysis is a promising pathway for storing renewable energy in chemical fuels, and its catalyst will play a pivotal role in advanced energy conversion technologies [2, 4]. Since Troostwijk and Diemann first observed the phenomenon of water electrolysis in 1789 [5], it has been the subject of extensive research over the past years.

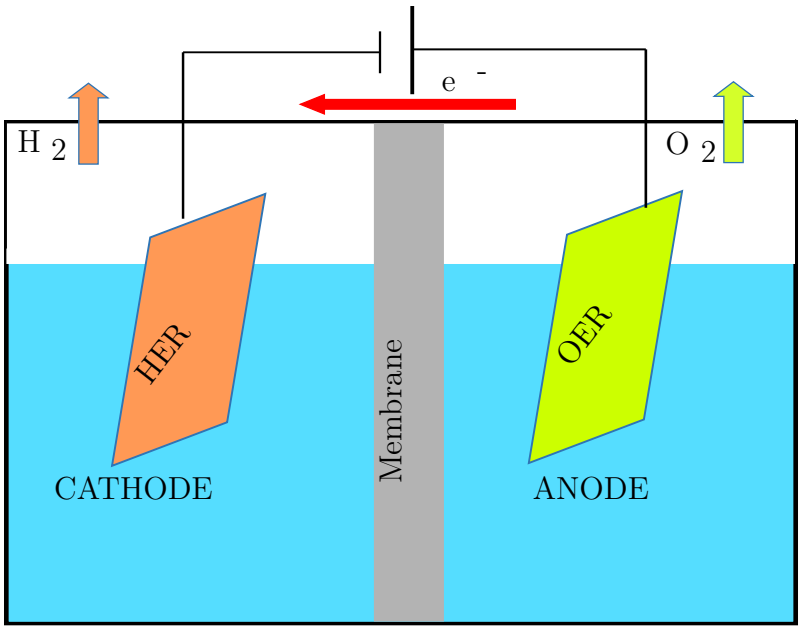

Figure 1.1: Water Electrolysis

1.1 Water Electrolysis

Water electrolysis has become increasingly important in the past decade due to its crucial role in energy conversion technologies such as water-splitting, rechargeable metal-air batteries, and fuel cells [3, 4]. The blueprint design of these systems may seem complex, but the core ideas are relatively easy to comprehend. It is a two-electrode system and a combination of two fundamental half reactions [2, 4], as shown in the Figure 1.1, where the energy from a renewable energy source like sunlight can drive the Hydrogen Evolution Reaction (HER) at the cathode and the Oxygen Evolution Reaction (OER) at the anode simultaneously [6]. Theoretically, a potential difference of 1.23 V between the anode and cathode is required to drive the overall reaction [7]. However, in a practical water electrolyzer much higher voltage is needed [8].

HER is a two-electron transport process involving electrochemical H^+ adsorption and desorption of H_2, requiring an overpotential (η_c) to proceed. In contrast, OER is an inherently more complex process. It has sluggish oxygen evolution kinetics since it needs to transfer four electrons through multi-step reactions with single-electron transfer at each step [9], where water molecules oxidize into four protons (H^+) and oxygen molecules (O_2) in acidic conditions, and hydroxyl groups (OH^-) are oxidized and transformed into H_2O and O_2 in the primary environment [4]. The cathodic and anodic half reactions under acidic and alkaline conditions are as follows.

Total Water oxidation reaction/water splitting reaction:

$$2H_2O \rightarrow 2H_2 + O_2$$

Acidic Conditions:

$$\text{Cathode Reaction : } 4H^+ + 4e^- \rightarrow 2H_2$$

$$\text{Anode Reaction : } 2H_2O \rightarrow O_2 + 4H^+ + 4e^-$$

Alkaline Conditions:

$$\text{Cathode Reaction : } 2H_2O + 4e^- \rightarrow 2H_2 + 4OH^-$$

$$\text{Anode Reaction : } 4OH^- \rightarrow 2H_2 + 2H_2O + 4e^-$$

The water oxidation reaction creates an oxygen double bond (O=O) by removing four protons from the water molecule [10], and the low activity of water oxidation at low potential is a significant obstacle for water splitting [11]. Thus, OER becomes a bottleneck reaction in the overall water electrolytic process as the energy accumulates at a multi-step transfer process of electrons and protons, leading to sluggish kinetic due to high overpotential (η_a), which is required to overcome the kinetic

barrier of OER to occur [12, 13, 14] as shown in Figure 1.2. The overpotential is the extra voltage required beyond the thermodynamic potential to drive a reaction at a rate that is fast enough to be practical for real-world applications. It arises from various sources of resistance and kinetic barriers within the electrochemical cell. Hence, developing effective and stable OER electrocatalysts by improving oxygen electro-kinetics can significantly improve energy-conversion efficiency [8].

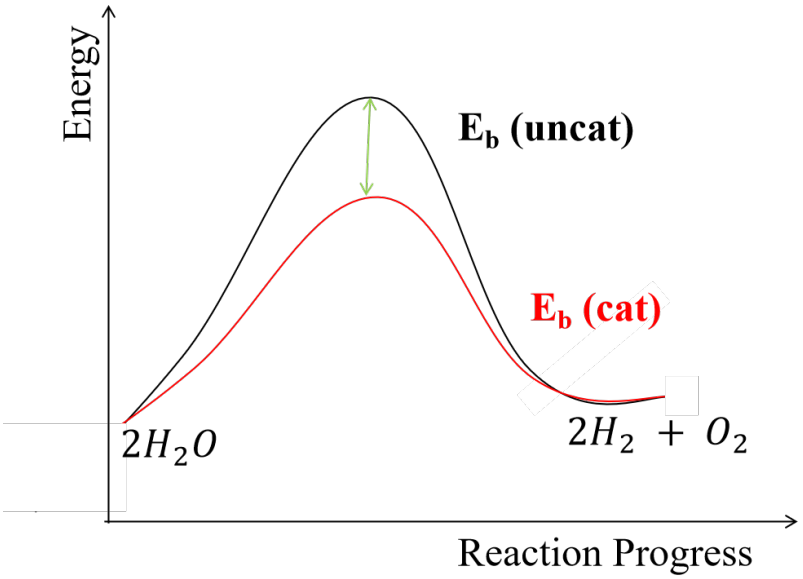

Figure 1.2: The energy barrier with and without catalyst

1.2 Catalyst

To improve OER kinetics, it is crucial to reduce the overpotential and ensure high catalyst stability to withstand harsh conditions and maintain long-term performance. This is a key focus in advanced catalyst development. Noble metals and oxides are the most studied catalysts because of their high stability in all pH values [12]. Currently, Ir/Ru-based compounds are considered benchmark catalysts for OER because of their relatively low potential and high stability, outperforming platinum (Pt) and Palladium (Pd) [15, 16]. As for oxides, iridium oxide (IrO_2) and ruthenium oxide (RuO_2) are regarded as the state-of-the-art OER catalysts [17]. These two metal oxides have a rutile structure, with Ru and Ir in the center of the octahedral site and oxygen at the corners. It is reported that, with high anodic potential, RuO_2 and IrO_2 undergo further oxidation to form RuO_4 and IrO_3, respectively, and subsequent dissolution in the solution. However, IrO_2 has the edge over RuO_2 as it is more stable and can sustain at the higher anodic potential in both acidic and alkaline conditions [18, 19]. Researchers comprehensively compared Ru, RuO_2, Ir, and IrO_2 as thin film electrodes in both acidic and basic solutions. Cherevko *et al.* reported that the activity decreases in the order of Ru > Ir ≈ RuO_2 > IrO_2, while the dissolution of the catalyst increases in the order of IrO_2 < RuO_2 < Ir < Ru [18].

Transition metal electrocatalysts are another class of materials that have attracted significant interest due to their affordability, abundance of resources, and superior corrosion resistance. Studies show that these materials can even outperform the noble-metal-based electrocatalysts in alkaline conditions [20, 21]. The ability to exist in a multi-valent oxidation state, as it is proved that the $M^{+2/+3/+4}$ states are the active sites for OER, making them tuneable for OER applications [22]. The OER activities of these materials are highly dependent on the structure, composition, oxidation state, and enthalpy for the lower to higher oxide transition [23]. Researchers have extensively studied the OER activity of metal oxide catalysts containing transition metals. This includes exploring various metal oxide families, such as perovskite, spinel, and layered (oxy)hydroxides, which have been confirmed to exhibit remarkable OER activity.

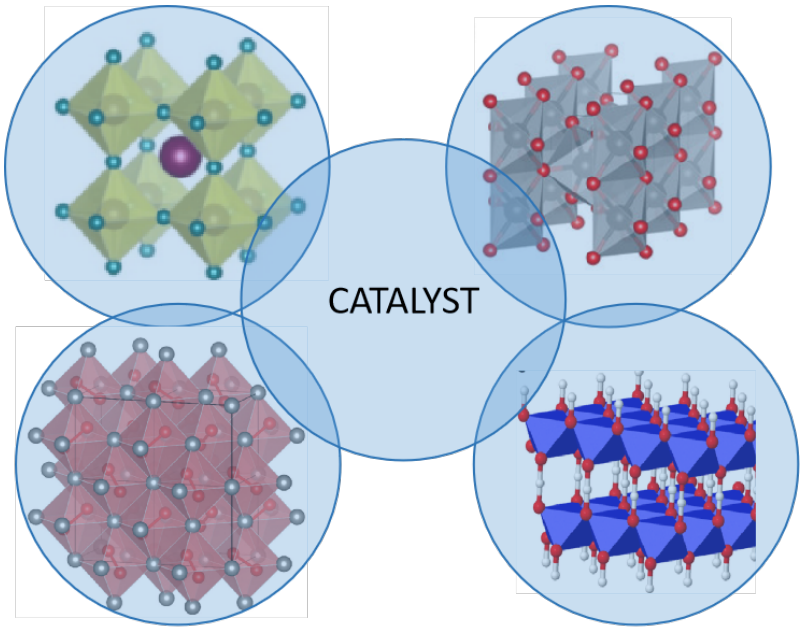

Figure 1.3: Electrocatalyst of different materials

1.3 Background: Iridium oxides-based catalyst

Given the potential of IrO_2 as an electrocatalyst, it is interesting to explore the properties of iridium-based catalysts, mainly IrO_2 and IrOOH. Iridium's electronic structure as a $5d$ transition metal is one of the reasons for its remarkable catalytic characteristics for the oxygen evolution reaction (OER). Iridium's $5d$ orbitals can better overlap with oxygen's p orbitals because they are more spatially stretched than lighter transition metals' $3d$ and $4d$ orbitals. This increases the reaction's efficiency by making it easier for bonds to form and break during the catalytic cycle [24, 25]. Moreover, the strong spin-orbit coupling in $5d$ transition metals like iridium is crucial in stabilizing various oxidation states, essential for catalytic activity. As any transition metal, iridium can exist in multiple oxidation states (primarily $Ir^{+3/+4}$) [26]. IrOOH is not much researched yet, but so far, it is reported that

it resembles layered hydroxides and is typically synthesized through ion-exchange processes, transforming precursors like $K_{0.75}Na_{0.25}IrO_2$ into IrOOH by reacting with hydrochloric acid [26]. The resulting material retains a layered structure similar to brucite ($Mg(OH)_2$) but with distinctive iridium-based layers [27]. Several studies have carried out its catalytic activity, which demonstrates large current densities at relatively low overpotential, and its remarkable stability makes it acceptable for long-term use in proton exchange membrane (PEM) electrolyzers [28, 29]. Reactive oxygen species within its structure are crucial for enhancing its catalytic performance due to its efficiency in facilitating multiple proton-coupled electron transfer (PCET) steps. Moreover, the dynamic nature of the iridium framework enables it to cycle through various oxidation states (Ir^{+3} and Ir^{+4}), which is essential for the OER mechanism.

1.4 Aim

Given the limited computational studies on layered IrO_2 and IrOOH, this thesis uses theoretical modeling techniques, such as density functional theory (DFT) calculations, to accurately model Ir-based oxides and oxyhydroxides to predict the structural, electronic, and vibrational properties that can provide insights into their catalytic mechanism. Previous DFT studies of IrO_2 have been limited to the local density approximation (LDA) and generalized gradient approximations (GGA), e.g., PBE or PBEsol [25, 27, 30] and hybrid functionals (B3PW91 and PBE0) [25]. Different structures of IrO_2 are reported with no theoretical evidence to prove its dynamical stability. This prompted us to investigate the dynamical stability of IrO_2 and IrOOH by employing various computational techniques, including different hybrid functionals, van-der Waals corrections, and spin-orbit coupling, and it is found that the system exhibits imaginary modes in the phonon dispersion relation, which correspond to phonon instabilities in the materials. In this thesis, we aim to address the challenges associated with computational modeling of the layered IrO_2 and IrOOH structures. We examine different computational setups for accurately modeling these materials and determine their structural, vibrational, and electronic properties. We believe these insights will contribute to future research on the design and prediction of the properties of layered Ir-based materials for OER applications.

2

Theory

Using theoretical and computational techniques to understand material behavior at an atomistic level has resulted in the development of computational modeling as a vital tool for comprehending and predicting material properties. In condensed matter physics and materials research, computational modeling, particularly density functional theory (DFT), allows researchers to investigate electronic structures, geometric optimizations, and phonon dispersions. The principles of quantum mechanics have provided the fundamental framework for understanding the behavior of electrons in atoms, molecules, and solids. Therefore, material theory has been increasingly influenced by computer simulations that use a quantum-mechanical approach.

The first step in computational modeling is to solve the many-body Schrödinger equation, which describes the quantum mechanical behavior of a system. However, solving the Schrödinger equation exactly is computationally intractable for interacting many-body systems because of their complexity in accounting for all particle interaction. Early attempts to solve the many-body Schrödinger equation began in 1928 with D.R. Hartree [31], who introduced the self-consistent field (SCF) method, in which one solves the equation numerically for each electron moving in a central potential due to the nucleus and other electrons [32]. This method assumes that each electron is distinguishable from the others and moves independently in an averaged field created by all other electrons, simplifying calculations. However, electrons are indistinguishable spin-1/2 particles, or fermions, and the approach ignores the Pauli exclusion principle, that two fermions cannot occupy the same quantum state because the many-fermion wave function must be antisymmetric during particle exchange. Vladimir Fock improved on this in 1930 [33] by introducing a Slater determinant to antisymmetrize the wave function, resulting in the Hartree-Fock (HF) approach. However, the HF approach ignores electron correlations while excluding magnetic interactions and relativistic effects, resulting in inaccurate total energy and electron distributions. Additionally, it is computationally costly when large systems are investigated.

Thomas [34] and Fermi [35] independently proposed an alternative approach in 1927 and 1928, respectively, to address the limitations of the HF method. Their approximation treated the kinetic energy as an explicit function of the electron density, while considering the nuclear-electron and electron-electron interactions in a purely classical manner. This model treated electrons as noninteracting particles in a homogeneous gas with a density equal to the local electron density at any given

point, resulting in a more computationally feasible framework for modeling electronic behavior. This motivated Hohenberg and Kohn [36] to formulate the Hohenberg-Kohn (HK) theorems in 1964, which provided a solid theoretical foundation for Density Functional Theory (DFT). They proved that all one needs is the electron density, a variable earlier introduced by Thomas and Fermi, which contains all the information about the ground state properties of a system. Building on this, Walter Kohn and Lu Jeu Sham [37] 1965 developed practical equations that made DFT a valuable tool. Their approach simplified the problem by modeling a system of non-interacting particles with the same electron density as the real system, making it much easier to study complex materials.

In this thesis, we use DFT to investigate the structural properties of IrO_2 and IrOOH. IrO_2, or iridium oxide, is known for its excellent catalytic properties and stability, making it a candidate for various industrial applications. IrOOH, a hydroxylated form of IrO_2, is modeled by adding hydrogen atoms to the optimized structure of IrO_2. This research focuses on studying their geometrical optimization, electronic properties, and phonon dispersion using different exchange-correlation functionals. By using DFT, this work aims to provide valuable insights into the structure of IrO_2 and IrOOH, potentially guiding future experimental and theoretical studies.

2.1 Many-Body Schrödinger Equation

Let us envision a scenario where we wish to outline the properties of some well-defined collection of atoms. The basic idea is to know their energy and how their energy changes when we move the atoms around. At the atomic level, matter is defined as a collection of nuclei and electrons that interact via electrostatic forces [38]. In principle, the features of a collection of interacting, non-relativistic particles are entirely characterized by their many-body state $|\Psi(t)\rangle$, determined as a solution to the time-dependent Schrödinger equation [39].

$$i\hbar\frac{\partial}{\partial t}|\Psi(t)\rangle = H|\Psi(t)\rangle, \tag{2.1}$$

Where H is the system's Hamilton operator, it describes the evolution of the wave function Ψ for a particle in time and space. The time-independent Schrödinger equation determines the Hamilton operator

$$H|\Psi\rangle = E|\Psi\rangle, \tag{2.2}$$

correspond to allowed energies E of the system [39]. In principle, all properties of such a system can be derived from the quantum mechanical wavefunction of the full system $\Psi(r_1, r_2, ..., R_1, R_2, ...; t)$, where r_i and R_i denotes coordinates of the electron and nuclei in the system respectively [38].

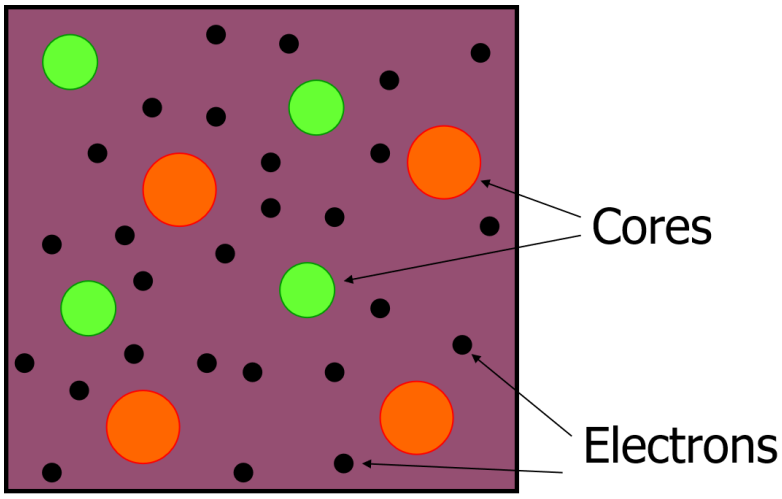

Figure 2.1: Complex many body problem

In a system with N electrons and M atomic nuclei, the position-space representation of the Hamilton operator in Hartree nuclear units ($\hbar = e = m_e = 4\pi\epsilon = 1$) is

$$\hat{H}_{\text{tot}} = \hat{T}_N + \hat{T}_e + \hat{W}_{NN} + \hat{W}_{ee} + \hat{W}_{Ne} \tag{2.3}$$

$$\begin{aligned} H_{\text{tot}} = &-\sum_I \frac{\hbar^2}{2M_I}\nabla^2_{\mathbf{R}_I} - \sum_i \frac{\hbar^2}{2m_e}\nabla^2_{\mathbf{r}_i} + \frac{1}{2}\sum_{\substack{I,J \\ I\neq J}} \frac{Z_I Z_J e^2}{|\mathbf{R}_I - \mathbf{R}_J|} \\ &+ \frac{1}{2}\sum_{\substack{i,j \\ i\neq j}} \frac{e^2}{|\mathbf{r}_i - \mathbf{r}_j|} - \sum_{I,i} \frac{Z_I e^2}{|\mathbf{R}_I - \mathbf{r}_i|}. \end{aligned} \tag{2.4}$$

To obtain solutions to the above equation, we must convert the problem from a many-body system to a one-body system. The intention is to reduce the complexity of the system by introducing approximations. Suppose one gives rise to a certain approach where the resulting equations are free of adjustable parameters. In that case, this method is commonly called *ab initio* or *first principles method* [39].

2.1.1 Born-Oppenheimer Approximation

The task at hand to solve Eq.(2.3) for the Hamilton operator in Eq.(2.4) is impossible if no approximations are considered. The common starting point in solving and simplifying many-body problems is to treat the electrons and ionic degree of freedoms separately [38]. Electron and lattice dynamics can be decoupled due to the much larger mass of lattice ions, which implies that the dynamics of the heavy nuclei are much slower than those of the electrons. Thus, the nuclei kinetic energy term is treated as a perturbation, and ion-ion repulsion is simply a continuous shift of the Hamilton operator [39]. This treatment is known as the *Born-Oppenheimer Approximation*.

The approximation simplifies the electronic Hamilton operator as

$$H_e = -\frac{1}{2}\sum_i \nabla_i^2 + \sum_{i\neq j}\frac{1}{|\mathbf{r}_i - \mathbf{r}_j|} + V_{\text{ext}}\,. \tag{2.5}$$

Similarly, a distinct Schrödinger equation can be derived for the nuclei, describing ionic motion in a homogeneous electron sea. A full-fledged quantum mechanical treatment is often unnecessary, as the nuclei can be approximated as classical particles evolving through the potential derived from the electronic Hamiltonian operator [39].

$$H_e\Psi_e\left(\{\mathbf{r}_i\};\{\mathbf{R}_I\}\right) = E_e\Psi_e\left(\{\mathbf{r}_i\};\{\mathbf{R}_I\}\right), \tag{2.6}$$

Although the Born-Oppenheimer approximation simplifies the many-body Schrodinger equation by treating electron's and nuclei's motion separately, the challenge remains unsolved. The complexity arises from the Coulombic interactions between electrons, which create a many-body problem that cannot be easily simplified without further approximations.

2.1.2 Hartree-Fock Approximation

In quantum chemistry and condensed matter physics, the HF approximation is an essential approach for solving the many-electron Schrödinger equation. It assumes that a single Slater determinant can approximate the many-electron wavefunction, ensuring the antisymmetry needed to satisfy the Pauli exclusion principle. The HF approach approximates the complex interactions between electrons by treating each one as if traveling through an average field produced by all the other electrons. As a result, the problem is reduced to resolving a number of orbital self-consistent field (SCF) equations.

Mathematically, the total electronic wavefunction $\Psi(\mathbf{r}_1, \mathbf{r}_2, \ldots, \mathbf{r}_N)$ in the HF approximation is represented as a Slater determinant:

$$\Psi(\mathbf{r}_1, \mathbf{r}_2, \ldots, \mathbf{r}_N) = \frac{1}{\sqrt{N!}}\begin{vmatrix} \psi_1(\mathbf{r}_1) & \psi_2(\mathbf{r}_1) & \ldots & \psi_N(\mathbf{r}_1) \\ \psi_1(\mathbf{r}_2) & \psi_2(\mathbf{r}_2) & \ldots & \psi_N(\mathbf{r}_2) \\ \vdots & \vdots & \ddots & \vdots \\ \psi_1(\mathbf{r}_N) & \psi_2(\mathbf{r}_N) & \ldots & \psi_N(\mathbf{r}_N) \end{vmatrix}.$$

The energy minimization of this wavefunction leads to the Hartree-Fock equations:

$$\left(-\frac{1}{2}\nabla^2 + V_{\text{ext}}(\mathbf{r}) + V_{\text{H}}(\mathbf{r}) + V_{\text{X}}(\mathbf{r})\right)\psi_i(\mathbf{r}) = \epsilon_i\psi_i(\mathbf{r}),$$

with

$$V_{\text{H}}(\mathbf{r}) = -\frac{Z}{|\vec{r}|} + \int \frac{n(\vec{r}')}{|\vec{r} - \vec{r}'|}\,d\vec{r}'. \tag{3.20}$$

Where $V_{\text{H}}(\mathbf{r})$ is the Hartree potential representing the Coulomb interaction, and $V_{\text{X}}(\mathbf{r})$ is the exchange potential arising from the antisymmetry of the wavefunction. Though powerful, the HF method neglects electron correlation effects, limiting its accuracy for systems with significant correlation. Post-Hartree-Fock methods,

such as Configuration Interaction (CI) and Coupled-Cluster (CC) theory, or Density Functional Theory (DFT), are often employed to account for these correlations and improve upon the HF approximation [40, 41].

2.1.3 Thomas-Fermi Model

The limitations of the HF approach prompted Thomas and Fermi to seek an alternative method for solving many-body problems. They developed an early approximation for the kinetic and internal potential energies based on the concept of a uniform electron gas, a hypothetical system with constant electron density. Their approach focused primarily on the kinetic energy while treating the nucleus-electron and electron-electron interactions in a fully classical manner.

$$T[\Psi] \approx T_{\mathrm{TF}}[n] = C_F \int n^{5/3}(r)\, dr \tag{2.7}$$

where C_F is a constant determined by the calculation and $n(\mathbf{r})$ is the electron density. We can also make the simple approximation of the internal potential energy, U by using the expression for a classically repulsive gas (i.e., completely ignoring electron correlations)

$$U[\Psi] \approx J[n] = \frac{e^2}{2} \iint \frac{n(\mathbf{r}_1)n(\mathbf{r}_2)}{|\mathbf{r}_1 - \mathbf{r}_2|}\, d\mathbf{r}_1\, d\mathbf{r}_2 \tag{2.8}$$

combining the classical expression for the nuclear-electron attractive potential and the electron-electron repulsive potential, we have the famous Thomas-Fermi expression for the energy of an atom,

$$E_{\mathrm{TF}}[n(\vec{r})] = \frac{3}{10}(3\pi^2)^{2/3} \int n^{5/3}(\vec{r})\, d\vec{r} - Z \int \frac{n(\vec{r})}{r}\, d\vec{r} + \frac{1}{2} \iint \frac{n(\vec{r}_1)n(\vec{r}_2)}{|\vec{r}_1 - \vec{r}_2|}\, d\vec{r}_1\, d\vec{r}_2 \tag{2.9}$$

The importance of this equation lies not in its ability to describe an atom's energy accurately but in the fact that the power is wholly expressed in terms of electron density. In other words, the equation specifies how to transfer a density onto an energy E with no more information needed. Consequently, establishing the framework for Density Functional Theory (DFT) [42, 43].

2.2 Density Functional Theory

The Schrödinger equation describes how electrons behave in atoms, molecules, and solids. The computational complexity of solving the many-body Schrödinger equation makes it difficult to create a strong numerical technique for determining the electronic structure. In 1964, Walter Kohn and Pierre Hohenberg formulated two theorems based on electron density and energy functionals, marking a pivotal moment in developing Density Functional Theory (DFT). However, Thomas-Fermi and Hartree−Fock (HF) can be regarded as forerunners of modern DFT [44]. DFT, employs electron density $n(\mathbf{r})$ as a fundamental variable [45] (a function of three

coordinate variables, $n(\mathbf{x}, \mathbf{y}, \mathbf{z})$) which drastically reduces the computational cost by converting a $3N$-dimensional equation (e.g., a description of 10 electrons requires 30 dimensions) to $\mathbf{n}$ separate 3-dimensional ones with the use of electron density [44].

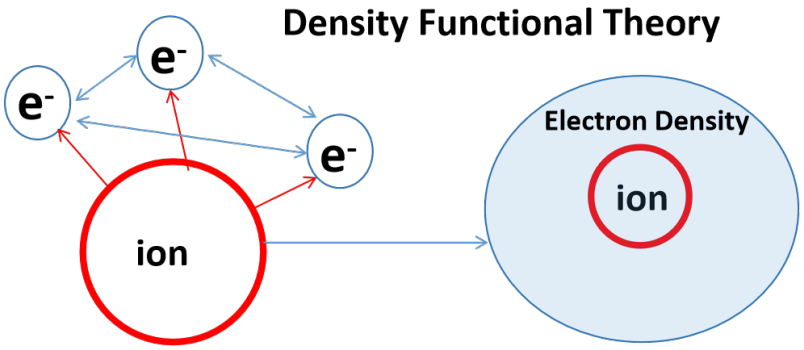

Figure 2.2: Schematic representation of Density Functional Theory (DFT)

2.2.1 Hohenberg-Kohn theorem

The Thomas–Fermi approach was developed to express energy exclusively in terms of electronic density [46]. However, the idea was intuitive then, but proof that this was the case had to wait more than thirty years when Hohenberg and Kohn (1964) [37] formulated and proved a theorem that put the former ideas on solid mathematical grounds. The theorem is divided into two parts, where the essential variable is the electron density $n(\mathbf{r})$ rather than the many-body wave function. Since the electron density only depends on three coordinate variables, it is much more tractable than the many-body wave function, independent of the number of electrons. This tactic is supported by Ref. [47], the first assertion of the theorem is that the ground-state electron density and the external potential correspond one to one. Therefore, the external potential can only be computed once the ground-state electron density is known [48]. To prove this, let us assume there exist two different external potentials $v_{\text{ext}}(\vec{r})$ and $v'_{\text{ext}}(\vec{r})$ which both yield the same ground state density $n_0(\vec{r})$. These two potentials result in different Hamiltonians H and H' which yield different ground states $|\Psi_0\rangle$ and $|\Psi'_0\rangle$. The corresponding ground state energies for these two systems are obtained via $E_0 = \langle\Psi_0|H|\Psi_0\rangle$ and $E'_0 = \langle\Psi'_0|H'|\Psi'_0\rangle$. By taking $|\Psi'_0\rangle$ as the trial ground state for the Hamiltonian H, one obtains the following inequality by the variational principle in quantum mechanics:

$$E_0 < \langle\Psi'_0|H|\Psi'_0\rangle = \langle\Psi'_0|H'|\Psi'_0\rangle + \langle\Psi'_0|H - H'|\Psi'_0\rangle = E'_0 + \int d^3x\, n_0(\vec{r})\,(v_{\text{ext}}(\vec{r}) - v'_{\text{ext}}(\vec{r}))\,. \tag{2.10}$$

Equivalently, one can take $|\Psi_0\rangle$ as the trial ground state ket for the Hamiltonian H' to obtain another inequality:

$$E'_0 < E_0 - \int d^3x\, n_0(\vec{r})\,(v_{\text{ext}}(\vec{r}) - v'_{\text{ext}}(\vec{r}))\,. \tag{2.11}$$

Adding the last two equations yields the following statement, which is the desired contradiction:

$$E_0 + E'_0 < E_0 + E'_0. \tag{2.12}$$

This is a contradiction; therefore, we conclude that the assumption that the densities are the same, which is incorrect. This proves that the ground state density uniquely determines the external potential $v_{\text{ext}}(\vec{r})$ within an additive constant. So, we conclude that the ground state wave function can be considered as a functional of the ground state density

$$\Psi_0(\vec{r_1}, \vec{r_2}, ..., \vec{r_N}) = \Psi[n_0(\vec{r})] \tag{2.13}$$

and the total energy of the system is a functional of the ground state electron density

$$E[n] = F[n] + V[n] = \langle \Psi[n] | \hat{H} | \Psi[n] \rangle, \tag{2.14}$$

where $F[n] = \langle \Psi[n] | \hat{T} + V_{ee} | \Psi[n] \rangle$

The second part of the Hohenberg-Kohn theorem, also known as the **variational principle**, states that the ground state energy of a many-electron system can be obtained by minimizing a functional of the electron density. Mathematically, if $E[n]$ is the energy functional that depends on the electron density $n(\vec{r})$, the correct ground state density $n_0(\vec{r})$ is the one that minimizes this functional:

$$E_0 = \min_{n(\vec{r})} E[n(\vec{r})]. \tag{2.15}$$

This implies that the exact ground state energy E_0 can be found by varying the electron density without solving the many-body Schrödinger equation directly. The proof of the second theorem is also simple. According to theorem 1, a system with ground state density $n_0(\vec{r})$ uniquely determines its external potential $V(\vec{r})$ and ground state wave function Ψ_0:

$$E[n_0(\vec{r})] = \langle \Psi_0 | \hat{H} | \Psi_0 \rangle = F[n_0(\vec{r})] + \int V(\vec{r}) n_0(\vec{r}) \, d\vec{r}.$$

Now, let us consider any other density $n'(\vec{r})$, which necessarily corresponds to a different wave function Ψ'. This would lead to

$$E_v[n'(\vec{r})] = \langle \Psi' | \hat{H} | \Psi' \rangle = F[n'(\vec{r})] + \int V(\vec{r}) n'(\vec{r}) \, d\vec{r} > \langle \Psi_0 | \hat{H} | \Psi_0 \rangle = E[n_0(\vec{r})]$$

Thus, the energy given by the equation 2.15 in terms of the Hohenberg-Kohn functional evaluated for the correct ground state density $n_0(\vec{r})$ is indeed lower than the value of this expression for any other density $n'(\vec{r})$ [49]. The inequality follows Rayleigh–Ritz's variational principle for the wave function but is applied to the electronic density. Therefore, the variational principle states that

$$\delta \left\{ E_V[n\vec{r}] - \mu \left(n(\vec{r}) \, d\mathbf{r} - N \right) \right\} = 0,$$

Which leads to a generalization of the Thomas–Fermi equation:

$$\mu = \frac{\delta E_V[n]}{\delta n} = v_{\text{ext}}(\mathbf{r}) + \frac{\delta F[n]}{\delta n}.$$

The knowledge of $F[n]$ implies the knowledge of the solution of the full many-body Schrödinger equation. It has to be remarked that $F[n]$ is a universal functional, which does not depend explicitly on the external potential. It depends only on the electronic density. In the Hohenberg–Kohn formulation, $F[n] = \langle\Psi|\hat{T} + \hat{V}_{\text{ee}}|\Psi\rangle$, where Ψ is the ground state many-body wave function. These two theorems form the mathematical basis of density functional theory or DFT [46].

2.2.2 Kohn and Sham Approach

In the Hohnberg-Kohn theorem, it is stated that the ground state energy of a many-electron system is a unique functional of the electron density $n(\vec{r})$

$$E_0 = \min_{n(\vec{r})} E[n(\vec{r})]. \tag{2.16}$$

The major problem is that the exact form of the functional $T(n(\vec{r}))$ is not known analytically as it contains the interaction between the electrons. Thus, one has to approximate somehow the functional $T(n(\vec{r}))$ to achieve reliable results for the ground state energy of the system [50]. The most desirable way to counter is finding a solution that allows iterations [51]. The earliest known efforts of an iterative approach are the self-consistent single-particle Hartree-Fock equations [52]. The HF method is fundamentally based on the wavefunction, approximating the complex many-electron wavefunction as a single Slater determinant. This approach allows HF to treat exchange interactions exactly but neglects the electron correlation, leading to limitations in accuracy.

2.2.2.1 Kohn-Sham System

Kohn and Sham, taking inspiration from the Hohnberg-Kohn theorem and SCF method of the Hartree-Fock approach, introduced "orbitals" as a way to approximate the kinetic energy functional by mapping the system of interacting particles onto a system of non-interacting particles with the same density [53]. This was done by constructing an effective external potential $v_{\text{eff}}^{KS}(\vec{r})$, which accounts for the interaction between the electrons. This potential is constructed such that the density $n(\vec{r})$ of the non-interacting system matches that of the interacting system. The KS equations are derived from minimizing the energy functional under the constraint that the total number of electrons is fixed [46, 43, 49]. The total energy functional $E[n]$ is expressed as:

$$E[n] = T_s[n] + \int v_{\text{ext}}(\vec{r})n(\vec{r})\,d\vec{r} + \frac{1}{2}\int\int \frac{n(\vec{r})n(\vec{r}')}{|\vec{r}-\vec{r}'|}\,d\vec{r}d\vec{r}' + E_{\text{xc}}[n]$$

Here:

- $T_s[n]$ is the kinetic energy of the non-interacting system.
- $v_{\text{ext}}(\vec{r})$ is the external potential, typically due to the nuclei.
- The second integral represents the Hartree energy, describing the classical electrostatic repulsion between electrons.

- $E_{\text{xc}}[n]$ is the exchange-correlation energy functional, which accounts for the many-body effects not captured by the other terms.

2.2.2.2 Kohn-Sham Equations

The Kohn-Sham (KS) equations are derived by minimizing the total energy functional with respect to the electron density, subject to the normalization constraint:

$$\sum_{i=1}^{N} \int |\phi_i(\vec{r})|^2 \, d\vec{r} = N$$

This leads to a set of self-consistent equations for the single-particle orbitals $\phi_i(\vec{r})$:

$$\left[-\frac{1}{2}\nabla^2 + v_{\text{KS}}(\vec{r})\right] \phi_i(\vec{r}) = \epsilon_i \phi_i(\vec{r})$$

where the effective Kohn-Sham potential $v_{\text{KS}}(\vec{r})$ is defined as:

$$v_{\text{KS}}(\vec{r}) = v_{\text{ext}}(\vec{r}) + \int \frac{n(\vec{r}')}{|\vec{r} - \vec{r}'|} \, d\vec{r}' + \frac{\delta E_{\text{xc}}[n]}{\delta n(\vec{r})}$$

In this formulation:

- $v_{\text{ext}}(\vec{r})$ represents the external potential, typically due to the nuclei.
- The second term is the Hartree potential, describing the classical electrostatic interaction between electrons.
- The last term involves the exchange-correlation potential, which accounts for the many-body effects beyond the classical description.

The orbitals obtained, ϕ_i, will be called KS-orbitals, their corresponding energies. ϵ_i will be called KS-orbital energies.

2.2.2.3 Self-Consistent Field Procedure

The Kohn-Sham equations are typically solved iteratively through a self-consistent field (SCF) procedure:

1. **Initial Guess:** Start with an initial guess for the electron density $n(\vec{r})$.
2. **Solve KS Equations:** Solve the KS equations to obtain the orbitals $\phi_i(\vec{r})$.
3. **Update Density:** Compute a new electron density from the obtained orbitals:
$$n(\vec{r}) = \sum_{i=1}^{N} |\phi_i(\vec{r})|^2$$
4. **Check Convergence:** Compare the new density with the previous one. If they are sufficiently close, the procedure is converged. Otherwise, update the density and repeat.

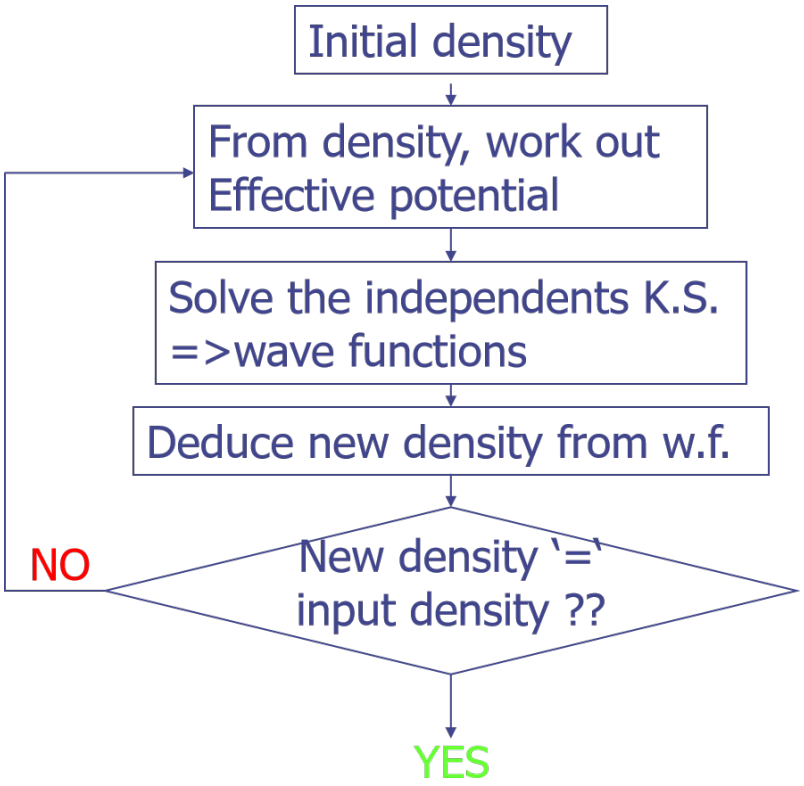

Figure 2.3: Flow chart of self-consistent field

Once the self-consistent electron density is obtained, the total energy of the system can be calculated using the energy functional:

$$E[n] = \sum_{i=1}^{N} \epsilon_i - \frac{1}{2} \int \int \frac{n(\vec{r})n(\vec{r'})}{|\vec{r} - \vec{r'}|} d\vec{r} d\vec{r'} + E_{\mathrm{xc}}[n] - \int \frac{\delta E_{\mathrm{xc}}[n]}{\delta n(\vec{r})} n(\vec{r})\, d\vec{r}.$$

In theory, all many-body effects are covered if we know the precise E_{xc} and V_{xc} $(= \frac{\delta E_{\mathrm{xc}}[n]}{\delta n(\vec{r})})$. The ability to find an approximation for the functional E_{xc} and determine if it is sufficiently accurate and simple are the only requirements for the practical development of DFT [54].

2.2.2.4 Exchange-correlation Functional

The exchange-correlation functional (E_{xc}) is not precisely known [54], and without it, the Kohn-Sham equations are unsolvable. Despite the lack of an exact XC energy functional E_{xc}[n(r)], effective approximations have been developed that are both simple and successful. These approximations reasonably predict many system properties and significantly lower computational costs, leading to the widespread use of DFT for electronic structure calculations [55]. Over the years, many approximations have been developed for the exchange-correlation function. Exchange-correlation (XC) functionals are broadly classified into several categories. These include local and semi-local functionals and functionals that incorporate non-local exchange. Some functionals are constructed to account for van der Waals (vdW) interactions. Additionally, doubly hybrid functionals combine density functional theory (DFT) with

elements from molecular mechanics and wavefunction-based methods.

2.2.2.5 Local and Semi-Local Functional

The earliest and simplest approximation is the **Local Density Approximation (LDA)**, which is extensively employed and can be described as an approximation method that relies on estimating the exchange-correlation energy (E_{xc}) at a given point in a system by considering the electron density only at that specific location, i.e. it can be seen as local and assumes that the density is regarded homogeneous everywhere [56].

$$E_{xc}^{LDA}[n(\mathbf{r})] = \int d\mathbf{r} n(\mathbf{r}) \epsilon_{xc}(n(\mathbf{r}))\Big), \tag{2.17}$$

where ϵ_{xc} is the energy density per electron at a point $\mathbf{r}$. Because of the homogeneous density assumption, LDA tends to overestimate binding energies and underestimate ionization and ground state energies of atoms [55]. A density gradient can be used to offset the mistake brought about by the non-homogeneity of the actual electronic density. **GGA**, or the **Generalized Gradient Approximation** functionals generally lead to improved molecular geometries [56], accuracy in total energies [57], atomization energies [57, 58, 59], energy barriers, and structural energy differences [60, 61, 62] compared to LDA [63].

$$E_{xc}^{GGA}[n(\mathbf{r})] = \int d\mathbf{r} n(\mathbf{r}) \Delta n(\mathbf{r}) \epsilon_{xc}(n(\mathbf{r})). \tag{2.18}$$

Two of the most widely used GGA functionals are Perdew-Burke-Ernzerhof (PBE)[63] and Perdew-Wang (PW91) [64] functional. However, several additional things could be improved, such as underestimating the band gap and overestimating the lattice constant for the heavier elements [56]. Meta-GGA functionals are a natural advancement from the GGA (generalized gradient approximation) functionals and may offer greater accuracy. In contrast to GGA, which only contains the density and its first derivative in the exchange-correlation potential, the original form of the meta-GGA DFT functional includes the second derivative of the electron density (the Laplacian) [65]. Some popular meta-GGAs include Becke95 correlation functional [66], TPSS [67], SCAN [68], and revM06-L [69].

2.2.2.6 Functionals with Non-Local and van der Waals Corrections

Functionals with non-local and van der Waals (vdW) corrections are used to precisely represent dispersion forces, which are important for explaining weak intermolecular interactions and other long-range phenomena. Unlike standard local or semi-local functionals, non-local vdW functionals, such as vdW-DF or VV10, include explicit terms to capture the long-range correlation energy resulting from dispersion interactions. These approaches make use of non-local correlation kernels, which allow for the seamless integration of vdW forces into the DFT framework without the need for empirical parameters. These non-local vdW-corrected functionals, when combined with robust exchange functionals derived from the Generalized Gradient

Approximation (GGA), provide a more physically grounded description of systems such as layered materials, molecular crystals, and surface adsorption. Their predictive power considerably boosts DFT's utility for applications where van der Waals forces dominate.

Nonlocal van der Waals (vdW) interactions, crucial for accurately describing noncovalent interactions, are challenging for local functionals and HF theory. High-level wavefunction-based methods like quantum Monte Carlo and CCSD(T) are accurate but computationally expensive. To address this, vdW correlations are added to density functionals, leading to vdW-DF functionals. These include a nonlocal correlation term:

$$E_c^{\mathrm{nl}} = \frac{1}{2} \iint d\vec{r} d\vec{r}' n(\vec{r}) \Phi(\vec{r}, \vec{r'}) n(\vec{r}')$$

where $\Phi(\vec{r}, \vec{r'})$ is the nonlocal correlation kernel. The VV10 functional, for example, uses an analytic form for $\Phi(\vec{r}, \vec{r'})$ that incorporates parameters fitted to benchmark vdW coefficients [70]. Popular vdW-DFs with nonlocal correlations include the Rutgers-Chalmers vdW-DF family, BEEF (GGA+nonlocal correlation) [71], and SCAN+rVV10. These functionals offer a practical balance between computational cost and accuracy for modeling complex interactions in chemical systems.

2.2.2.7 Empirical dispersion corrections (DFT-D)

Functionals with molecular mechanics dispersion (often abbreviated as DFT-D) are a class of density functional theory (DFT) methods that incorporate dispersion corrections. These corrections are vital for accurately describing van der Waals interactions, weak but significant forces between atoms and molecules that are not adequately captured by standard DFT functionals. Dispersion-corrected functionals add an empirical dispersion term to the conventional DFT energy expression. The total energy in DFT-D methods can be expressed as:

$$E_{\text{DFT-D}} = E_{\text{DFT}} + E_{\text{disp}} \tag{2.19}$$

Where:

- E_{DFT} is the standard DFT energy,
- E_{disp} is the dispersion correction term.

The dispersion correction E_{disp} is typically modeled using the form:

$$E_{\text{disp}} = -s_6 \sum_{i<j} \frac{C_6^{ij}}{R_{ij}^6} f_{\text{damp}}(R_{ij}) \tag{2.20}$$

Where:

- C_6^{ij} is the dispersion coefficient for the atom pair i and j,
- R_{ij} is the distance between atoms i and j,
- s_6 is a scaling factor that depends on the specific DFT functional used,

- $f_{\text{damp}}(R_{ij})$ is a damping function that avoids unphysical behavior at short distances.

An example of such a function is the DFT-D3 method, developed by Grimme *et al.* [72], which uses environment-dependent dispersion coefficients C_6^{ij} to improve accuracy across different chemical environments. DFT-D3 has significantly improved the accuracy of DFT calculations for systems involving weak interactions, such as molecular complexes, layered materials, and biomolecules. These functionals are essential for applications in fields where van der Waals forces play a crucial role, such as in studying adsorption phenomena, molecular crystals, and biomolecular interactions.

2.2.2.8 Jacob's Ladder

Perdew proposed a "Jacob's ladder" for density functional approximations [73], which is a ladder from the Earth (Hartree world) to Heaven (chemical accuracy) (Figure 1). according to the complexity of the exchange-correlation functionals. The first rung of the ladder is completed by the LSDA, which only depends on spin densities. GGAs and NGAs complete the second rung, adding the local spin density gradients to their constructions. The meta-GGAs are on the third rung, and spin kinetic energy densities and the Laplacians of densities are added to the constructions [74]. The fourth rung is more complex and completed by the hybrid density functionals, which contain a fraction of HF exchange. Doubly hybrid functionals complete the fifth rung, which employs the virtual orbitals for the exchange-correlation energy calculations (e.g., MP2 correlation energy).

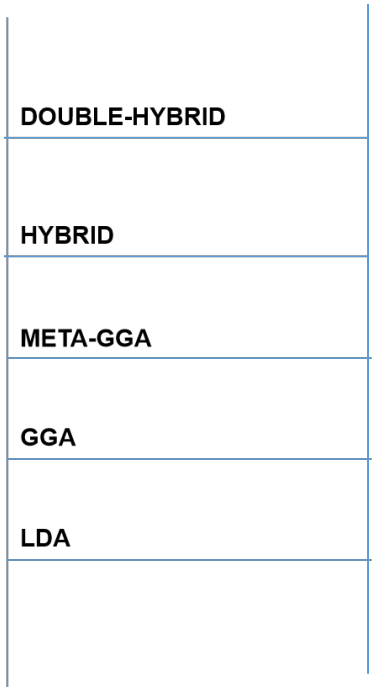

Figure 2.4: Schematic diagram of "Jacob's ladder" of exchange-correlation functionals proposed by J. P. Perdew.

2.3 Phonons

Phonons are quantized vibrations of atoms in a crystal lattice and play a central role in understanding the properties of materials. In solid-state physics, phonons arise from the collective oscillations of atoms around their equilibrium positions, and they can be thought of as the quantum mechanical version of classical vibrations. The dynamics of these vibrations can be captured using the equation of motion for the atoms in a lattice as

$$m\frac{d^2u_n}{dt^2} = -C(u_n - u_{n-1}) + C(u_{n+1} - u_n), \tag{2.21}$$

where m is the mass of the atom and u is the displacement of the corresponding atom. This equation of motion may be solved by assuming a wave solution,

$$u_n(t) = ue^{i(kan-\omega t)}. \tag{2.22}$$

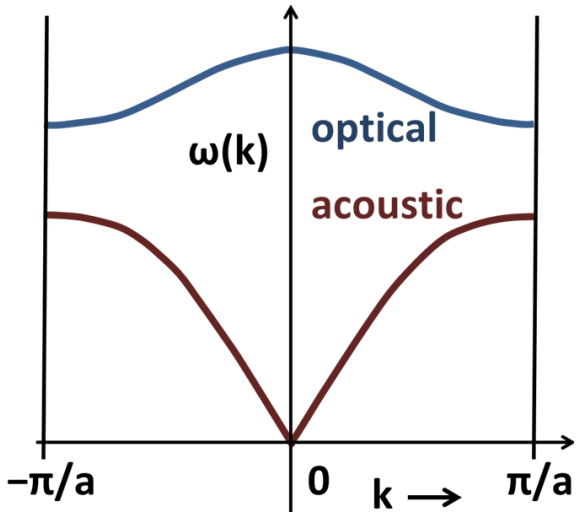

Figure 2.5: Phonon dispersion curves in linear diatomic chain

This wave is only defined in the lattice sites and has the frequency ω and the wave vector k. a corresponds to the distance between two neighboring atoms, and n is, as mentioned earlier, the number of atoms under consideration. Equation 2.21 can be solved by insertion of Equation 2.22, and from the solution, the phonon dispersion relation is extracted,

$$\omega(k) = 2\sqrt{\frac{C}{m}}\left|\sin\left(\frac{ka}{2}\right)\right|. \tag{2.23}$$

dispersion relations, which describe how the phonon frequency (*omega*) varies with the wave-vector (K). This relationship is essential for predicting lattice stability and detecting phonon instabilities, manifesting as imaginary frequencies in the phonon dispersion curves. These instabilities can indicate structural changes or phase transitions in materials.

2.4 Computational Details

The present thesis employs an electronic structure computation package based on DFT called *Vienna ab-initio simulation package* (VASP), created by Kresse *et al.* [75, 76, 77, 78, 79]. VASP uses a plane-wave basis-set code for ab initio density-functional calculations. Additionally, we used VASPKIT [80], which is an open-source command-line tool, that provides a reliable and user-friendly interface for conducting high-throughput analysis of various material characteristics using raw data generated by the VASP code. Plotting and analysis of ab initio solid-state calculation is carried out by open-source Python library PYMATGEN [81] and python toolkit SUMO [82]. PHONOPY package is used for the phonon calculations [83, 84].

Using (VASP), first-principle simulations within density functional theory are carried out to explore the structural and electrical characteristics of Iridium oxide and oxyhydroxide. The potentials employed are plane wave projector-augmented wave (PAW)[85], rVV10 van der Waals (vdW) correction is consistently applied to the exchange-correlation functional *GGA Perdew–Burke–Ernzerhof (PBE)* functional [86] and meta-GGA functional *Strongly Constrained and Appropriately Normed functional (SCAN)* [68]. The energy cutoff of 520 eV is chosen for the plane-waves basis set. 10^{-6} eV is used as the convergence criterion between the subsequent electronic steps. All our calculations in the thesis are spin-polarized. In addition, spin-orbit coupling calculations are performed to examine its impact on the structural and electronic properties of the layered IrO_2 and IrOOH. For the phonon calculations, the kinetic energy cutoff is set to 600 eV.

3

Results and Discussion

IrO_2 crystallizes in a hexagonal primitive lattice (hP) with space group P-3m1 (number 164), characteristic of the trigonal crystal system. The unit cell is characterized by lattice parameters $a \approx b$ and c.

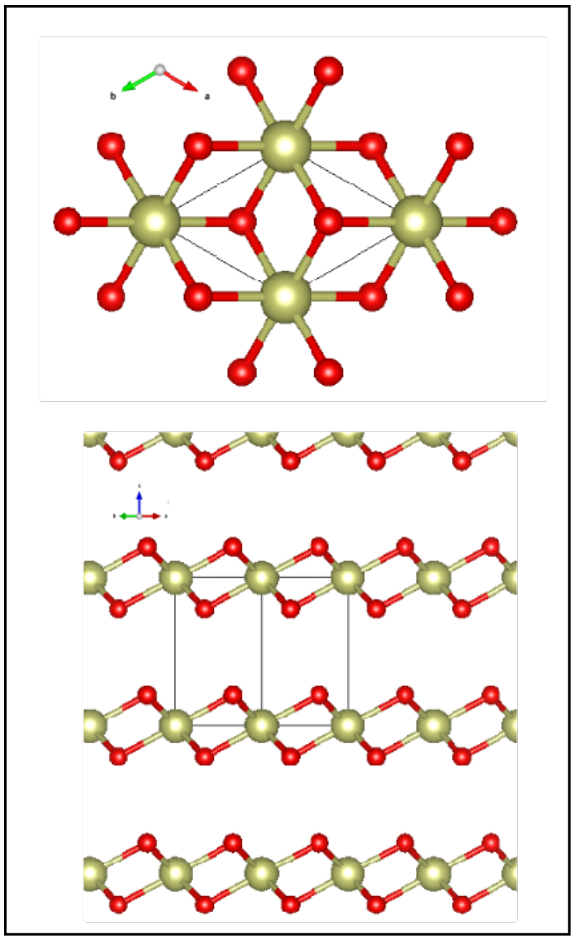

Figure 3.1: The structure of IrO_2 and it's Crystallographic

Most studies on IrO_2 have focused on the conventional rutile structure, which has been extensively characterized experimentally and computationally. In recent studies, layered IrO_2 structures have gained interest due to improved catalytic properties thanks to a high surface-to-body ratio. Here, we investigate layered IrO_2 structures that belong to the trigonal crystal system. These alternative structures can present distinct characteristics in terms of their stacking arrangement and lattice parame-

ters. Such variations could impact the material's electronic and structural properties. The IrO_2 structure we investigate here is composed of 1T-IrO_2 layers where a central Ir atom in a hexagonal unit cell that is coordinated with six oxygen atoms, resulting in a layered octahedral configuration. The layers are stacked perpendicular to the *c*-axis with weak interlayer interactions. The crystal structure of IrO_2 is shown in Figure 3.1

3.1 Structural Optimization

The optimized structure of materials can differ depending on various factors. The selection of exchange-correlation functional is one of these factors that could affect the accuracy and the efficiency. While a widely-used semi-local functional, PBE, is computationally inexpensive, often overestimates the structural parameters, leading to underestimated band gaps. For more accurate predictions without a significant increase in the computational cost, meta-generalized gradient approximation (meta-GGA) can be used. Moreover, the accuracy can be improved by better accounting of the dispersion forces. Here, we perform the geometrical optimization of layered IrO_2 structures using DFT with various exchange-correlation functionals, including PBE, PBE+D2, PBE+D3, PBE+rVV10L, and SCAN+rVV10.

Recent advances in van der Waals (vdW) corrections to semilocal density functional approximations, such as the revised Vydrov–van Voorhis nonlocal correlation functional (rVV10) [87], have attracted significant attention for studying layered transition metal oxides. SCAN+rVV10, which combines the strongly constrained and appropriately normed (SCAN) meta-GGA for short- and intermediate-range interactions with the long-range vdW interaction from rVV10, has proven particularly effective. This functional is constructed for general geometries, delivering excellent performance across various systems, including molecular complexes, solids, benzene adsorption on metal surfaces, and layered materials. It is reported to perform relatively better than the currently available methods but at a fraction of the computational cost [88]. This makes it highly suitable for computational studies of layered materials.

Another exchange functional of focus in this study is PBE+rVV10L, where the "L" denotes its optimization for layered materials. PBE+rVV10L has been reported to provide excellent accuracy for various properties in theoretical studies of layered materials. Although PBE+rVV10L may not be as versatile as SCAN+rVV10, it achieves comparable accuracy for crucial properties, such as lattice constants, bulk modulus, and cohesive energy, in strongly bound and hexagonal layered solids. Additionally, PBE+rVV10L is cheaper in computation and numerically more stable thanks to the much simpler mathematical form of PBE. While SCAN+rVV10 is more sophisticated and slightly more accurate, PBE+rVV10L remains a high-efficiency alternative that delivers reliable results, especially when computational resources are limited. Both functionals have been implemented in widely used *ab initio* codes, offering convenient and effective solutions for studying layered materials

Functionals	**Ir-Ir (a≈ b)(Å)**		**Ir-O** (Å)		**c** (Å)	
	WO-SOC	SOC	WO-SOC	SOC	WO-SOC	SOC
PBE	3.164	3.165	2.030	2.035	4.858	4.803
PBE+D2	3.174	3.178	2.022	2.027	3.735	3.746
PBE+D3	3.152	3.153	2.024	2.029	4.210	4.184
PBE+rVV10L	3.140	3.141	2.019	2.029	3.898	3.909
SCAN+rVV10	3.128	3.129	2.008	2.029	4.073	4.074

Table 3.1: Lattice parameters of IrO_2 with and without SOC using various functionals.

[89].

The lattice parameters of IrO_2 with and without spin-orbit coupling (SOC) using various functionals as shown in Table 3.1 compares the distance between Iridium atoms in the a˘b plane (tetragonal lattice), the bond length between Iridium and Oxygen atoms, and The lattice parameter along the c-axis. The Ir–Ir distance ($a \approx b$) shows negligible changes between SOC and wo-SOC cases, with differences typically on the order of 0.001 Å for all functionals. Similarly, the Ir–O bond length shows minor variations, with differences ranging from 0.005 Å to 0.021 Å. The c lattice parameter exhibits slightly larger changes but remains within 0.011 Å to 0.055 Å across the functionals. Overall, the inclusion of SOC has a negligible impact on the structural parameters, indicating that SOC does not significantly affect the lattice structure of IrO_2 for these functionals, at the same time, SOC may have a more pronounced influence on other properties, such as electronic or vibrational behavior. In contrast, different functionals affect the lattice parameters of the structure, highlighting different electron-electrons treatment with vdW-corrections.

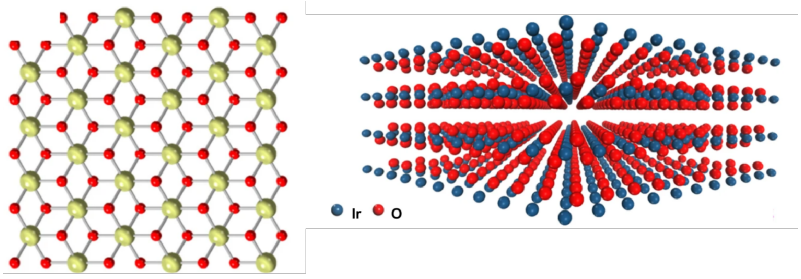

Figure 3.2: (a) Model of 1T-IrO_2 (b) Schematic of layered 1T-IrO_2

The structure as shown in Figure 3.2 corresponds to the 1T phase of IrO_2 in the Dang, Qian et al. (2021) [90]. The 1T phase differs significantly from the more common rutile phase of IrO_2, which has a tetragonal structure. The optimized IrO_2 structure, mainly using SCAN+rVV10 and PBE+rVV10L, aligns closely with the basal plane dimensions 1T-IrO_2. The Ir−O bond lengths are consistent with experimental expectations of 2 Å.

3.2 Stacking Investigation

In layered materials, various arrangements of different stackings can greatly influence their properties and behaviors. Therefore, we conduct a throughout computational investigation and examine various possible stackings to achieve a complete picture. The different stacking as shown in Figure 3.3, in a 1×1×2 supercell of optimized 2T-IrO_2, where the structure is arranged in a fashion where each layer is shifted relative to the adjacent layers by a translation vector as shown in Figure 3.3.

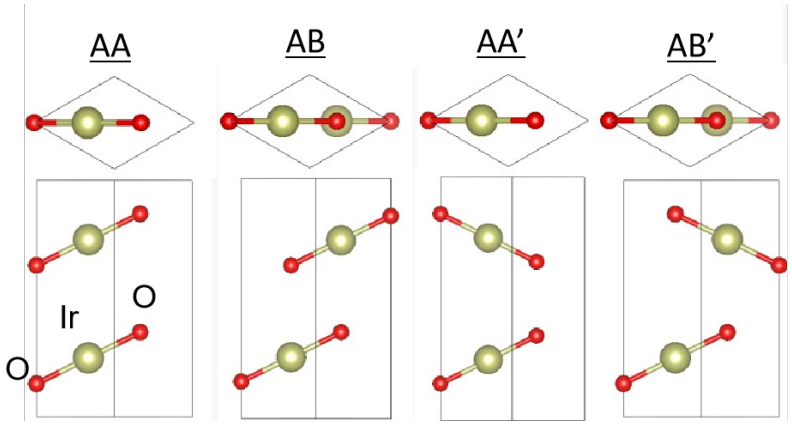

Figure 3.3: Illustration of AA, AB, AA′, and AB′ stacking configurations for IrO_2 and IrOOH structures. The top views (upper panels) show the relative positions of atoms in different layers, while the side views (lower panels) highlight the stacking along the c-axis. In AA stacking, atoms align directly on top of each other, maintaining symmetry. AB stacking introduces a lateral shift between alternating layers, changing interlayer interactions. AA′ stacking involves a slight distortion in one layer, breaking the perfect alignment while maintaining some symmetry. AB′ stacking features a mirror shift between alternating layers, further modifying interlayer interactions and symmetry

The Table 3.2 presents the results of energy optimization for various IrO_2 stacking configurations (AA, AB, AA′, AB′) using two functionals: PBE+rVV10L and SCAN+rVV10, both with and without SOC. The results consistently indicate that AA stacking is the lowest energy configuration for both functionals. Given the small magnitude of the energy difference between AA and AB′ stackings suggests that both stackings are competitive structures and could coexist under certain conditions. Thus, within the relative energy tolerance, both stackings are nearly degenerate. In the context of IrO_2, as shown in Table 3.2, the AA stacking configuration is the reference point with the lowest energy, set to $\Delta E = 0$ meV/atom.

The minimal energy differences, particularly between AA and AB′ stacking, which exhibit an energy difference as small as $\Delta E = +2$ meV/atom for PBE+rVV10L (without SOC) and nearly zero for SCAN+rVV10 (with SOC), suggest that IrO_2 might exhibit a low-energy barrier for transitioning between the AA and AB′ stacking arrangements. This observation implies the potential for the formation of stack-

Stacking	PBE+rVV10L (meV/atoms)		SCAN+rVV10 (meV/atoms)	
	WO-SOC	SOC	WO-SOC	SOC
AA	$\Delta E = 0$	$\Delta E = 0$	$\Delta E = 0$	$\Delta E = 0$
AB	$\Delta E = +27$	$\Delta E = +26$	$\Delta E = +24$	$\Delta E = +16$
AA'	$\Delta E = +47$	$\Delta E = +48$	$\Delta E = +37$	$\Delta E = +34$
AB'	$\Delta E = +2$	$\Delta E = +4$	$\Delta E = +9$	$\Delta E = +0.2$

Table 3.2: Energy optimization of IrO2 stackings

ing faults, which occur when there is a disruption in the ideal stacking order of atomic layers. Stacking faults are known to arise when the energy barrier between different stacking sequences is small, allowing for a spontaneous shift in the relative positioning of layers. In our system, the close energy proximity between the AA and AB′ stackings could result in structural defects in the form of stacking faults. This could indicate that the material could switch between these stackings without a significant energy penalty, potentially leading to structural or dynamic changes in the material. Observing such slight energy differences reinforces the importance of considering stacking faults in modeling IrO_2. Understanding these faults could provide insight into the dynamic stability and structural flexibility of IrO_2 under operational conditions and their potential impact on the performance of Ir-based catalysts.

3.3 Comparison of band gap with and without Spin-Orbit Coupling (SOC)

The comparison of band structures with and without spin-orbit coupling (SOC) for IrO_2 reveals that introducing SOC leads to band splitting particularly in SCAN+rVV10 near the Fermi level, though not as evident in PBE+rVV10L SOC lifts the degeneracy between spin-up and spin-down states, which means energy levels that were previously identical are now split apart. Additionally, SOC causes energy level shifts, slightly altering the position of the electronic bands. These changes are especially pronounced in functional SCAN+rVV10, underscoring the importance of including SOC in systems with heavy elements such as Iridium. It indicates its suitability for systems where both strong correlation effects and relativistic interactions are significant, and without accounting for SOC, the band structure might show degenerate (unsplit) states. Despite the inclusion of SOC, all functionals consistently predict that IrO_2 maintains its metallic nature, with bands crossing the Fermi level as shown in Figure 3.4.

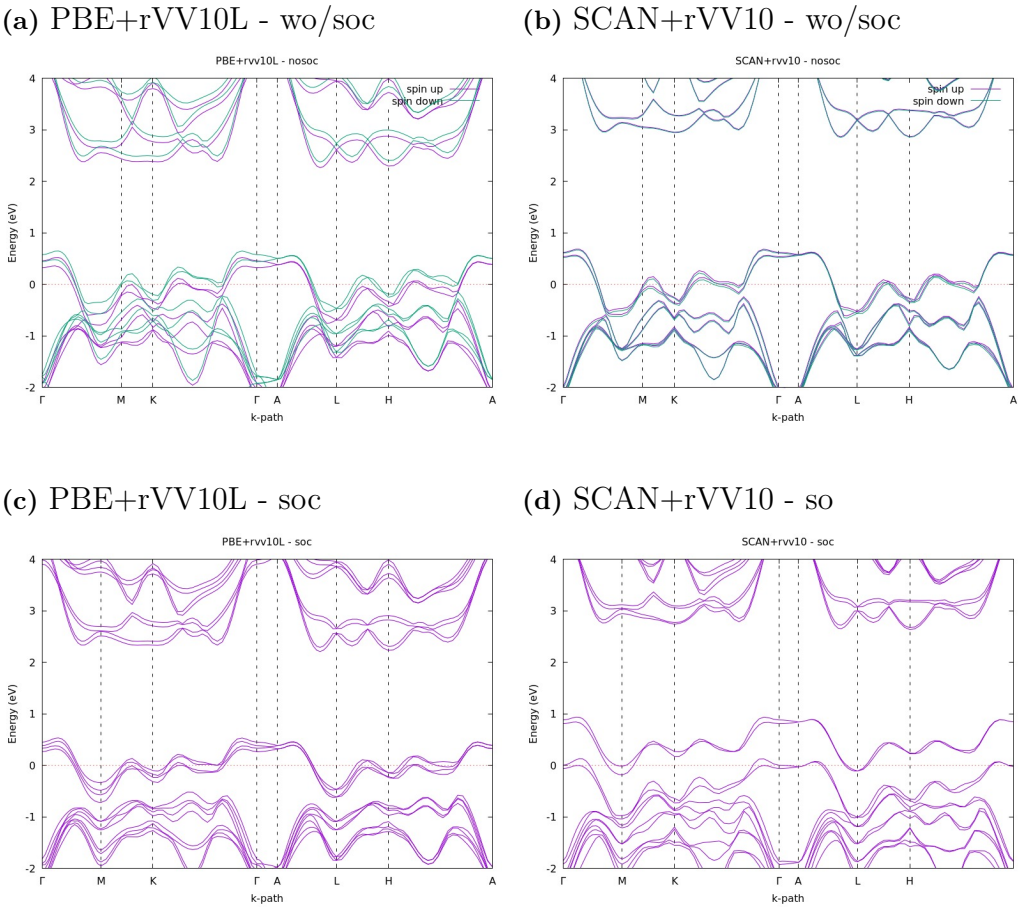

Figure 3.4: Comparison of band structures with and without SOC

3.4 Structure Stability - Phonon Dispersion

Phonon calculations are critical for understanding the dynamic stability of crystal structures, especially at low temperatures (0 K), as they provide insights into the vibrational modes of a material. These calculations are essential for assessing whether a structure is dynamically stable or unstable by examining the presence or absence of imaginary modes in the phonon dispersion. In this thesis, phonon dispersion analysis is particularly important to evaluate the dynamic stability of IrO_2 structures optimized using different exchange-correlation functionals.

The phonon dispersion calculations in our study revealed distinct differences in terms of the dynamical stability of the IrO_2 structures between the two functionals used. For SCAN+rVV10, the phonon dispersion shows several imaginary modes, particularly near the Γ, K, and A points in the Brillouin zone, indicating that the structure is dynamically unstable. Conversely, the phonon dispersion obtained using PBE+rVV10L shows no imaginary frequencies along the k-path, indicating that the structure is dynamically stable at 0 K across all regions of the Brillouin zone. Several strategies can be explored to address the presence of imaginary modes in the

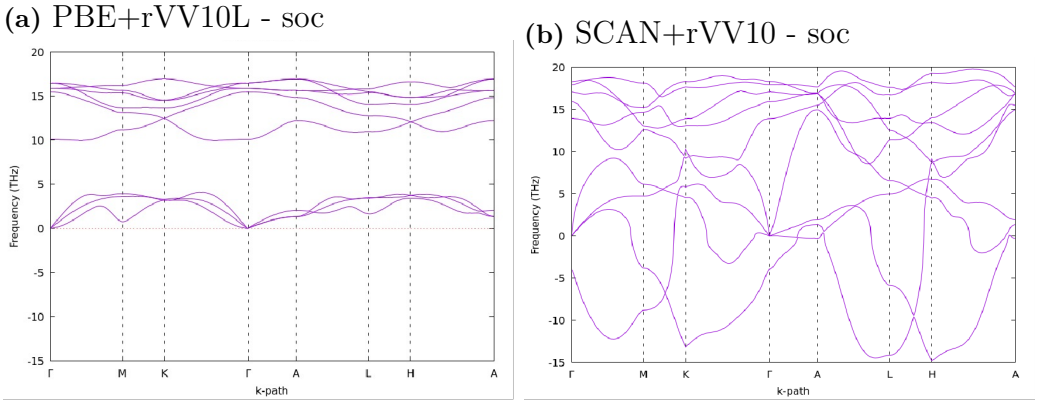

Figure 3.5: Comparison of phonon dispersion between PBE+rVV10L and SCAN+rVV10 with SOC

SCAN+rVV10 phonon dispersion. One approach is applying random displacements to atomic positions in a supercell to better sample the potential energy surface. Another possibility is to displace atoms based on the imaginary phonon modes.

3.5 Distorted IrO_2 structure

Here, to uncover a new structural configuration that achieves dynamical stability, we applied random displacements on the atomic coordinates in a 2×2×2 IrO_2 supercell and optimized structures with SCAN+rVV10 and PBE+rVV10L. As a result, we discovered a distorted IrO_2 phase, as shown in Figure 3.6. The distorted IrO_2 structure adopts a *triclinic* Bravais lattice (aP) with space group *P1* (number 1), which indicates the absence of any symmetry elements such as inversion, rotation, or reflection.

In contrast, the first IrO_2 structure exhibits a hexagonal Bravais lattice (hP) with a space group P-3m1 (number 164), characterized by much higher symmetry. The key difference between the two structures lies in their symmetry and the resulting atomic arrangement. While the hexagonal structure is more uniform, the distorted triclinic structure exhibits a broader range of bond lengths and angles, indicating greater structural flexibility. This flexibility may make the distorted structure more prone to rearrangements by accommodating shifts in atomic positions, and also allow it to stabilize under certain conditions, such as at different pressures or temperatures. Next, to check its dynamical stability, we carry out phonon calculations on the distorted structure. Phonon dispersions with both PBE+rVV10L and SCAN+rVV10 show no imaginary modes (see in Figure 3.7), confirming that introducing the distortions to the pristine structure makes the new distorted structure dynamically stable.

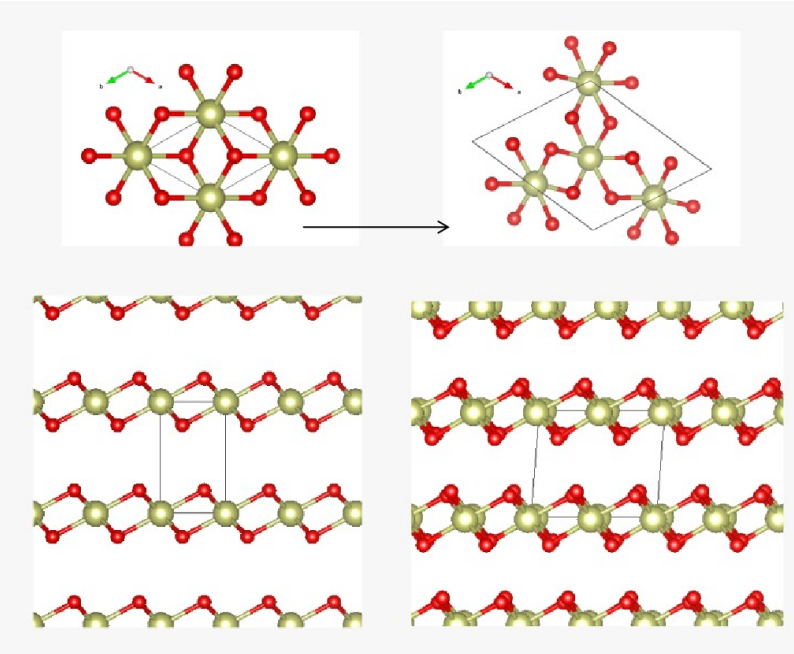

Figure 3.6: The distorted structure of IrO_2

Parameter	Value
a	6.291 Å
b	5.596 Å
c	4.291 Å
α	87.443
β	86.530
ζ	116.102
Unit Cell Volume	135.020 $Å^3$
Space Group	P-1 (No. 1)

Table 3.3: Lattice parameters, bond length, and unit cell volume of the distorted IrO_2.

3.6 Comparative Analysis of Distorted and Pristine IrO_2 Structures

Confirming that the distorted IrO_2 structure is dynamically stable for both functionals, we now analyze the different stacking of the distorted IrO_2 layers. In the energy analysis of the IrO_2 stacking configurations, as depicted in the Table 3.4, it is evident that the stability of the structures varies significantly depending on both the stacking order and the exchange-correlation functional employed. A comparison of PBE+rVV10L and SCAN+rVV10 functionals highlights important differences in how structural distortions influence the total energy.

In comparing the stability of different IrO_2 stacking configurations using the PBE+rVV10L and SCAN+rVV10 functionals, we find that both functionals con-

Stacking	**PBE+rVV10L (meV/atoms)**		**SCAN+rVV10 (meV/atoms)**	
	pristine	distorted	pristine	distorted
AA	$\Delta E = 5$	$\Delta E = 0$	$\Delta E = 0$	$\Delta E = 7$
AB	$\Delta E = 31$	$\Delta E = 6$	$\Delta E = 16$	$\Delta E = 9.5$
AA'	$\Delta E = 53$	$\Delta E = 11$	$\Delta E = 34$	$\Delta E = 15$
AB'	$\Delta E = 9.00$	$\Delta E = 5$	$\Delta E = 0.2$	$\Delta E = 9.2$

Table 3.4: Total DFT energy comparison between pristine and distorted IrO_2 structure with SOC

sistently predict the AA stacking as the most energetically favorable configuration. However, they differ slightly in their preference for whether the pristine or distorted form is more energetically favorable. In PBE+rVV10L, the distorted AA stacking is the lowest energy state, followed closely by the pristine AA stacking (5 meV/atom) and the distorted AB stacking (6 meV/atom). On the other hand, SCAN+rVV10 predicts the pristine AA stacking as an energetically favorable state, while the distorted AA stacking has a relative energy of 7 meV/atom. Interestingly, the pristine AB′ stacking in SCAN+rVV10 is almost as stable as AA stacking, with only a 0.2 meV/atom difference. In contrast, AA′ and AB′ stackings are highly unstable when distorted in PBE+rVV10L, showing massive energy penalties over 31 meV/atom and 53 meV/atom respectively, while SCAN+rVV10 shows more flexibility with distortions, leading to much more minor energy penalties. Overall, both functionals agree that AA stacking is the most energetically favorable structure with PBE+rVV10L favoring the distorted form, whereas SCAN+rVV10 favors the pristine form.

(a) PBE+rVV10L - soc

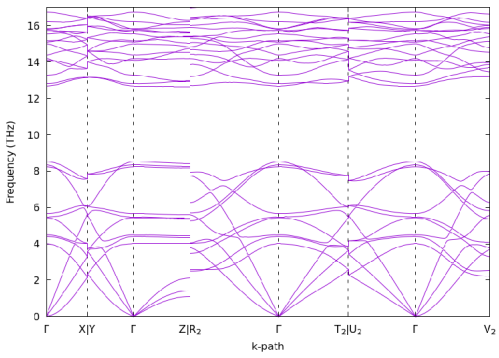

(b) SCAN+rVV10 - soc

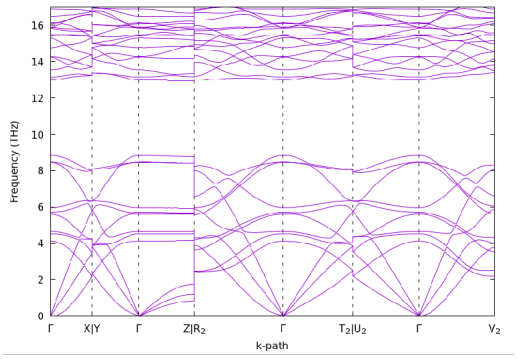

Figure 3.7: Comparison of phonon dispersion between PBE+rVV10L and SCAN+rVV10 with SOC for distorted structure

As for phonons dispersion comparison, for PBE+rVV10L, both the pristine and distorted structures exhibit no imaginary phonon modes, suggesting dynamic stability

for both structures. However, in the case of SCAN+rVV10, the pristine structure shows significant instability, with imaginary phonon modes observed near the Γ-point, suggesting it could be a local minimum rather than a global minimum. In contrast, the distorted structure eliminates these imaginary modes, indicating that the distortion stabilizes the structure dynamically. This could imply that the distortion dynamically stabilizes the structure, but it also suggests that SCAN+rVV10 may not accurately calculate forces, resulting in the absence of imaginary modes in the distorted structure. This creates a discrepancy between the energy and dynamic stability predicted by the SCAN+rVV10 functional where dynamic stability and energy minimization do not align.

(a) PBE+rVV10L **(b)** SCAN+rVV10

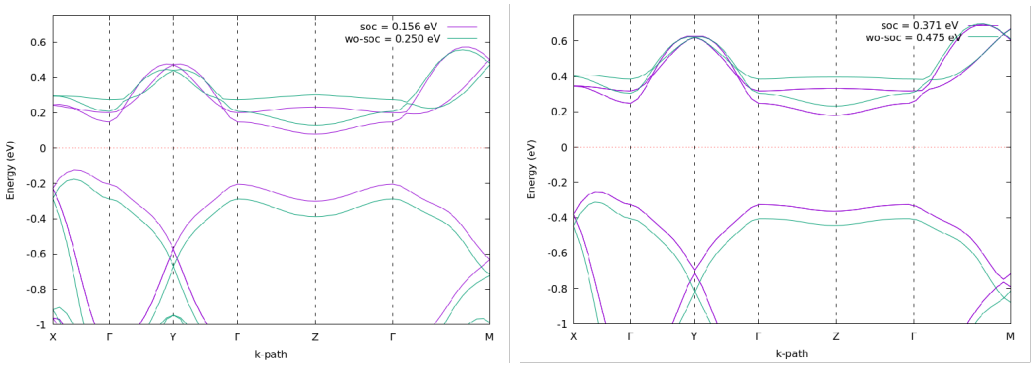

Figure 3.8: Comparison of band structure between PBE+rVV10L and SCAN+rVV10 with and without SOC for distorted structure

Compared to the pristine structure, the band structure of the distorted IrO_2 shows significant changes. The pristine IrO_2, using PBE+rVV10L and SCAN+rVV10, behaves as a metal, with bands crossing the Fermi level and no band gap opening. In contrast, the distorted structure is a semiconductor, as presented in the electronic band structures in Figure 3.8, with a band gap of 156 meV with PBE+rVV10L, and 371 meV with SCAN+rVV10 (with SOC). This suggests that the distortion introduces a localization effect, changing the electronic environment and reducing the overlap between the valence and conduction bands. Additionally, SOC has a stronger effect on the distorted structure than the pristine, where the gap is more noticeably narrowed. This comparison highlights how structural distortions in IrO_2 significantly alter its electronic properties, transforming the material from metallic in its pristine form to semiconducting in the distorted form, with the exact band gap size dependent on the functional and the inclusion of SOC.

3.7 Modeling of IrOOH

The results of IrO_2 lay the groundwork for the transition to IrOOH, where hydrogenation of IrO_2 will be investigated to determine how the introduction of hydrogen

affects both the structural and electronic properties and whether similar stability trends emerge. In the investigation of IrOOH, we have chosen to continue with both the pristine and distorted structures using the same functionals, PBE+rVV10L and SCAN+rVV10. Hydrogen incorporation could introduce subtle changes to the interlayer interactions; exploring how both functionals perform across the two structural phases is essential. This approach will also help us determine which structure (pristine or distorted) and functional offers a better description of IrOOH's electronic, structural, and vibrational properties.

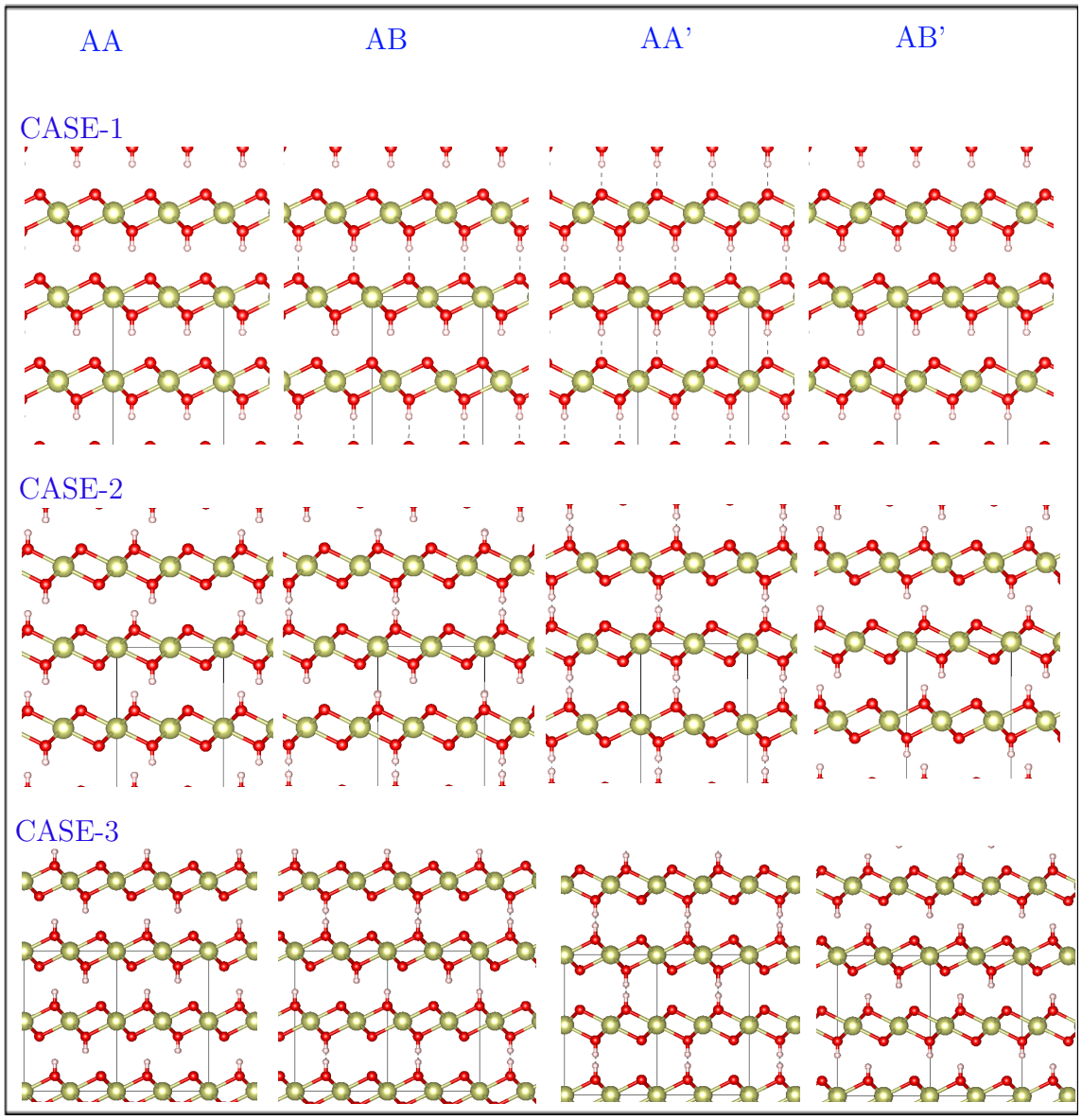

Figure 3.9: Initial structures of IrOOH of pristine structure

To investigate the structural and electronic properties of IrOOH, we divided the study into two key 'OH' configurations, cis and trans, across both the pristine and distorted IrO_2-based structures. The 'cis' configuration positions 'OH' groups on the same side of Iridium atoms within each layer. In contrast, the 'trans' configuration

places OH groups on opposite sides of the Iridium atoms affect the overall symmetry and alter interlayer interactions. we employed a 2×2×1 supercell for both structures' stacking arrangements to better capture layer interactions. we explored each configuration of various OH placements in pristine and distorted structures to scan all the possible configurations of IrOOH. The decision to include both structures stems from the observation that while the pristine structure maintains crystallographic symmetry, the distorted structure has shown stability in IrO_2 and may extend to IrOOH. Testing different OH configurations allows us to scan various IrOOH configurations across both structures. The supercell setup further allowed for detailed interaction analysis within a single layer (in-plane) and between different layers (out-of-plane), which are crucial for the computational modeling of a layered structure like IrOOH. Based on the geometric optimization of various IrOOH configurations with different stackings, we observed that many configurations converged to energetically and structurally similar states. This eliminated redundant or similar structures, streamlining the analysis to focus on three distinct cases based on their total DFT energy.

The basic blueprint in modeling IrOOH structure remains same for both pristine and distorted IrOOH as shown in Figure 3.9 and Figure 3.10. In analyzing the IrOOH system across different stackings (AA, AB, AA′, and AB′), we observe distinct trends in atomic displacements, shear angles, and energies that help understand the structure. The cis configurations generally exhibit smaller atomic displacements and minimal shearing, indicating that the atomic layers remain largely aligned. In contrast, the trans configurations show significantly larger atomic displacements, particularly for H and O atoms, as well as greater shear angles. During the optimization process to obtain a lower energy state, these features show notable layer shifts and in-plane reorganization. Such shifts suggest that the initial stacking is prompted to undergo structural adjustments driven by the interlayer interactions, particularly hydrogen bonding. This can be attributed to the structural feature where hydrogen atoms are sandwiched between oxygen atoms, facilitating interlayer bonding and stabilization of the sheared structure. Finally, the layer shifting represents a preference for more energetically favorable stackings, with the optimized structure minimizing energy via hydrogen bonding and layer flexibility.

3.8 Comparsion between pristine and distorted IrOOH structure

The initial distorted IrOOH structures post-optimization revert to a pristine-like IrOOH configuration suggests that the distortions introduced were energetically not optimal. This reversion indicates that the material inherently favors a more undistorted configuration, likely due to the strong bonding preferences between atoms. The hydrogen atoms, in particular, continue to position themselves between two oxygen atoms, a structural feature observed across distorted and pristine structures, highlighting the material's tendency to maintain this favorable arrangement. Another key observation is that IrOOH in both pristine and distorted prefers mirrored AA′ stacking, which differs from IrO_2 with most favorable stacking AA.

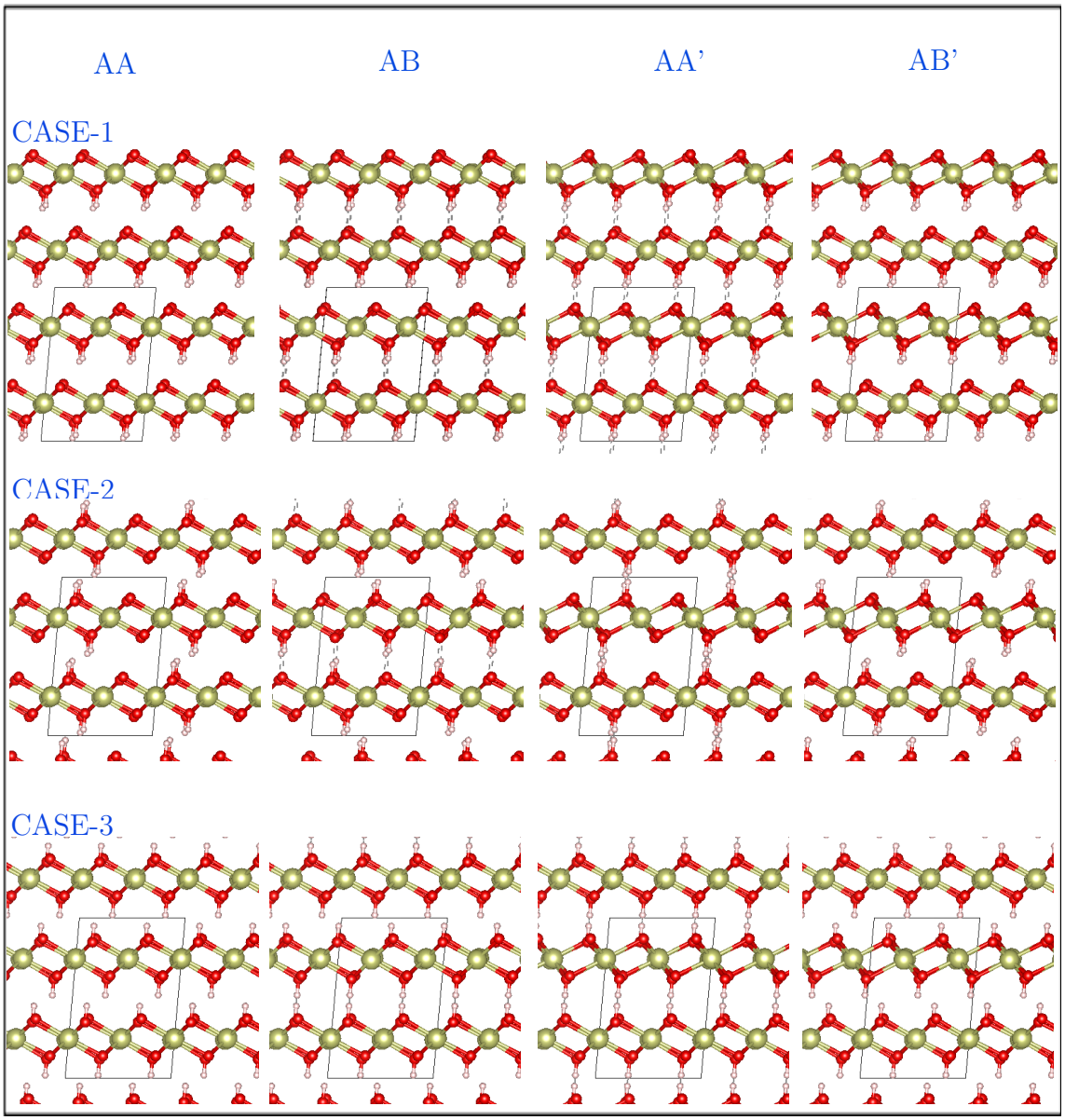

Figure 3.10: Initial structures of IrOOH of distorted structure

When comparing the pristine and distorted IrOOH structures, several key differences emerge. In the distorted structures, atomic displacements for Ir, O, and H are significantly larger, whereas the trans configurations are energetically more favorable. Overall, while the pristine IrOOH structure shows less distortion, the distorted structures demonstrate significant flexibility, especially in the trans configurations, with hydrogen's adaptability playing a crucial role in maintaining stability under distortion as shown in Figure 3.11.

Falling and other suggested [47] suggests that IrOOH adopts a 2H heterogeneity structure characterized by AB stacking, which closely aligns with the AA′ stacking configuration we have investigated. Both configurations break the perfect symmetry of AA stacking, resulting in altered local interactions. It describes the 2H hetero-

geneity model as belonging to the hexagonal space group $P6_3/mmc$, a common feature in layered materials like IrOOH. This structural similarity supports the relevance of the lowest energetically AA′ stacking model, as it captures key aspects of the 2H heterogeneity phase mentioned in the literature.

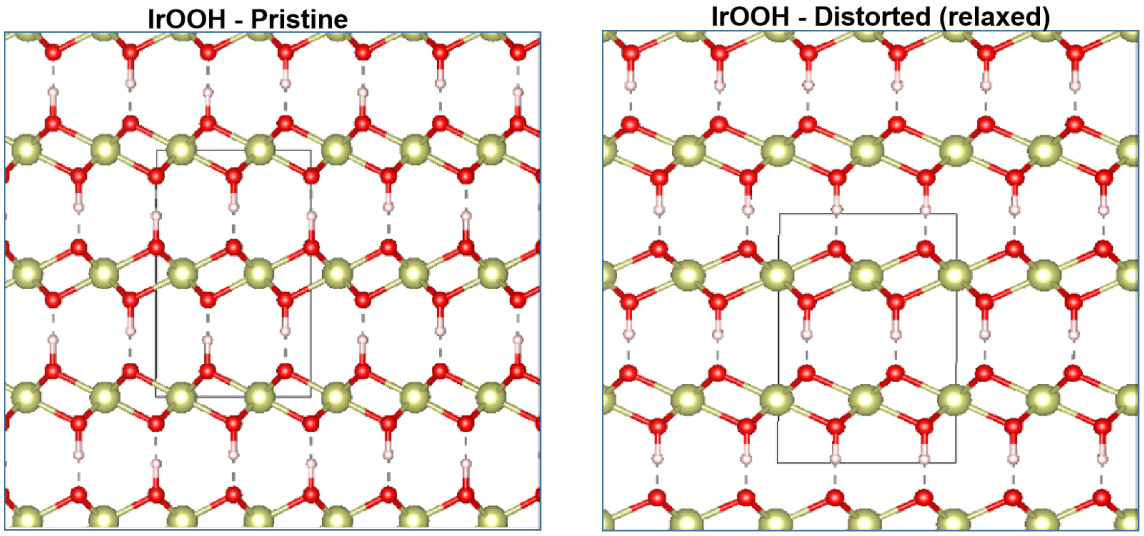

Figure 3.11: Lowest energy IrOOH configuration for pristine and distorted structure

The energy comparison between the two IrOOH structures as shown in Table 3.5 predicts the pristine IrOOH structure is the lowest energy configuration for both functionals, suggesting that the system prefers to remain in its undistorted form under these simulations. This indicates the high stability of pristine IrOOH compared to the distorted configurations. The fact that both functionals agree on this suggests a level of robustness in the calculations. The energy penalty for the distorted structure is relatively small (7-8 meV/atom), but it still indicates that inducing distortions in the IrOOH structure is energetically unfavorable. PBE+rVV10L and SCAN+rVV10 predict nearly the same energy trend, but SCAN+rVV10 predicts a slightly higher energy penalty for the distorted structure. This is consistent with the fact that SCAN is known for capturing more accurate descriptions of intermediate-range van der Waals interactions and may be more sensitive to structural changes.

Additionally, the band structure as shown in Figure 3.12 reveals a direct band gap of 1.752 eV for IrOOH, which is close to the experimental band gap of 1.9 eV reported by Falling *et al.* [47] and predicts to be a semiconductor as reported by Weber *et al.* [30]. While it also reports that DFT calculations typically underestimate the band gap (reporting a value of 1.3 eV), the band gap results between the computational and experimental values, indicating improved accuracy. This suggests that the functionals or corrections used (e.g., SCAN+rVV10 or PBE+rVV10L) effectively capture the electronic properties of IrOOH. The agreement between the calculated gap and experimental findings further validates our structural and electronic models of pristine IrOOH calculated using SCAN+rVV10 functional.

PBE+rVV10L (meV/atoms)		**SCAN+rVV10 (meV/atoms)**	
Pristine	Distorted	Pristine	Distorted
$\Delta E = 0$	$\Delta E = 7$	$\Delta E = 0$	$\Delta E = 8$

Table 3.5: Energy comparison between the lowest energy IrOOH configuration of pristine and distorted IrOOH respectively

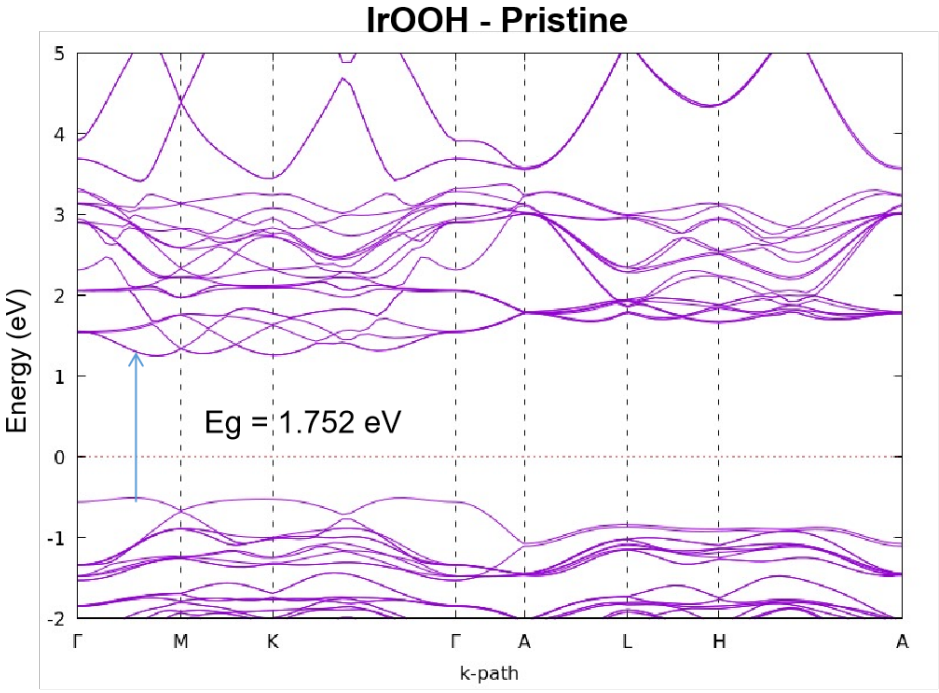

Figure 3.12: Band structure of pristine IrOOH

To compare the optimized structure with the experiment (orange) [26], we have performed theoretical (blue) XRD patterns for IrOOH which reveals a close match as shown in Figure 3.13, indicating that the theoretical model accurately captures the structural features of the material. Both patterns show sharp, well-defined peaks, with the strongest reflection around 10°, corresponding to the (001) plane, confirming the layered, hexagonal structure of IrOOH. The additional peaks in both patterns, such as (100), (101), and (102), further validate the well-ordered stacking along the *c*-axis. Minor shifts in peak positions and intensity between the two patterns are likely due to experimental factors, such as lattice strain, defects, or impurities, which are not fully accounted for in the theoretical model. The experimental XRD also shows a small impurity peak, absent in the theoretical pattern, suggesting a minor secondary phase that could arise from unreacted precursor material. Overall, the agreement between the theoretical and experimental results highlights the reliability of our theoretical model in predicting the crystalline structure of IrOOH,

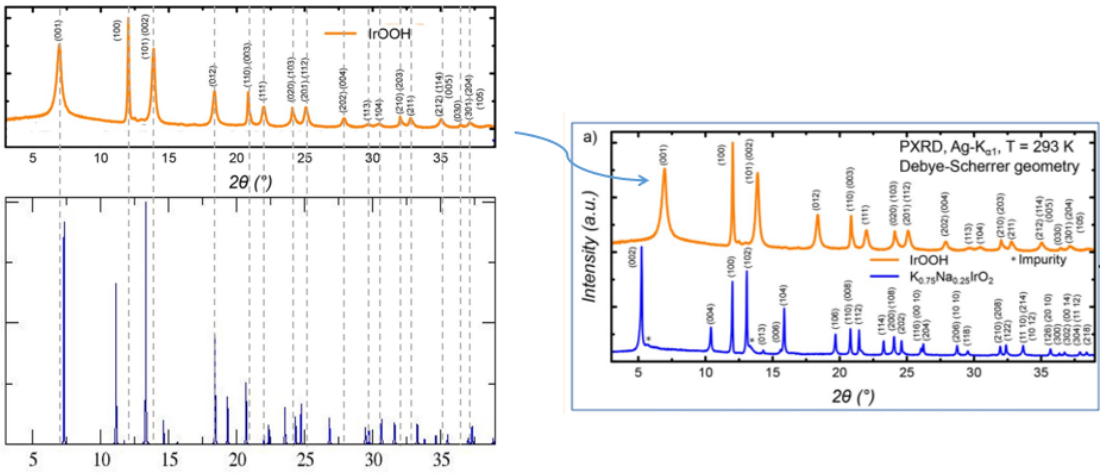

Figure 3.13: XRD comparison between experimental XRD and simulated theoretical XRD of IrOOH

while acknowledging small discrepancies due to real-world imperfections.

4

Conclusion

The computational study of IrO_2 and IrOOH reveals that the structural and electronic properties of IrO_2 are susceptible to both the choice of exchange-correlation functional and the presence of structural distortions. Across all calculations, the AA stacking configuration emerges as the lowest-energy arrangement, irrespective of the structure's functional or pristine or distorted nature. This suggests that AA stacking represents a robust structural configuration for IrO_2, while the minor energy differences between AA and AB' stackings imply that stacking faults are likely, which may influence the material's catalytic performance. The comparison between functionals highlights essential differences in their treatment of stability. PBE+rVV10L provides a dynamically stable description of IrO_2 with and without the need for structural distortions, making it a more computationally efficient and consistent choice for studying layered materials like IrO_2. In contrast, SCAN+rVV10, although more sophisticated and potentially more accurate, requires the introduction of distortions to maintain dynamic stability, particularly when investigating the material's vibrational properties through phonon calculations.

In terms of electronic properties, spin-orbit coupling (SOC) is crucial for accurately describing IrO_2's band structure, especially near the Fermi level, where SOC causes significant band splitting. This splitting is important for accurately modeling charge transport and catalytic activity for future research on Ir-based layered materials. Interestingly, structural distortions in IrO_2 can induce a transition from metallic to semiconducting behavior. In the case of IrOOH, semiconducting behavior is observed in both pristine and distorted structures. Meanwhile, distorted IrOOH reverts to a pristine-like structure, suggesting distortions in the IrOOH structure are energetically unfavorable, with the pristine structure being energetically favored. The X-ray diffraction (XRD) comparison between experimental and simulated results further validates the structural predictions made in this study, demonstrating strong agreement for layered IrOOH structures. This confirms the accuracy of the computational methods used and provides experimental support for the stability of the IrOOH under different stacking arrangements.

The computational framework we have selected in this thesis offers valuable insights into these materials' stability and electronic properties, laying the groundwork for future experimental validation and optimization. The potential for stacking faults, the role of SOC, and the transition to semiconducting properties through structural distortions highlight the versatility of IrO_2 and IrOOH as catalysts, providing a pathway toward improving their efficiency in green energy technologies.

Bibliography

[1] Nian-Tzu Suen, Sung-Fu Hung, Quan Quan, Nan Zhang, Yi-Jun Xu, and Hao Ming Chen. Electrocatalysis for the oxygen evolution reaction: recent development and future perspectives. *Chemical Society Reviews*, 46(2):337–365, 2017.

[2] Hongxia Wang, Kelvin HL Zhang, Jan P Hofmann, Freddy E Oropeza, et al. The electronic structure of transition metal oxides for oxygen evolution reaction. *Journal of Materials Chemistry A*, 9(35):19465–19488, 2021.

[3] Xiaobin Liao, Ruihu Lu, Lixue Xia, Qian Liu, Huan Wang, Kristin Zhao, Zhaoyang Wang, and Yan Zhao. Density functional theory for electrocatalysis. *Energy & Environmental Materials*, 5(1):157–185, 2022.

[4] Muhammad Tahir, Lun Pan, Faryal Idrees, Xiangwen Zhang, Li Wang, Ji-Jun Zou, and Zhong Lin Wang. Electrocatalytic oxygen evolution reaction for energy conversion and storage: A comprehensive review. *Nano Energy*, 37:136–157, 2017.

[5] S Trasatti. Water electrolysis: who first? *Journal of Electroanalytical Chemistry*, 476(1):90–91, 1999.

[6] Yan Jiao, Yao Zheng, Mietek Jaroniec, and Shi Zhang Qiao. Design of electrocatalysts for oxygen-and hydrogen-involving energy conversion reactions. *Chemical Society Reviews*, 44(8):2060–2086, 2015.

[7] Wesley T Hong, Marcel Risch, Kelsey A Stoerzinger, Alexis Grimaud, Jin Suntivich, and Yang Shao-Horn. Toward the rational design of non-precious transition metal oxides for oxygen electrocatalysis. *Energy & Environmental Science*, 8(5):1404–1427, 2015.

[8] Kexin Zhang and Ruqiang Zou. Advanced transition metal-based oer electrocatalysts: current status, opportunities, and challenges. *Small*, 17(37):2100129, 2021.

[9] Jiajia Song, Chao Wei, Zhen-Feng Huang, Chuntai Liu, Lin Zeng, Xin Wang, and Zhichuan J Xu. A review on fundamentals for designing oxygen evolution electrocatalysts. *Chemical Society Reviews*, 49(7):2196–2214, 2020.

[10] Xia Long, Jinkai Li, Shuang Xiao, Keyou Yan, Zilong Wang, Haining Chen, and Shihe Yang. A strongly coupled graphene and feni double hydroxide hybrid as an excellent electrocatalyst for the oxygen evolution reaction. *Angewandte Chemie International Edition*, 53(29):7584–7588, 2014.

[11] Yang Zhao, Fei Zhao, Xiaopeng Wang, Chenyu Xu, Zhipan Zhang, Gaoquan Shi, and Liangti Qu. Graphitic carbon nitride nanoribbons: graphene-assisted formation and synergic function for highly efficient hydrogen evolution. *Angewandte Chemie International Edition*, 53(50):13934–13939, 2014.

[12] Muhammad Tahir, Nasir Mahmood, Lun Pan, Zhen-Feng Huang, Zhe Lv, Jingwen Zhang, Faheem K Butt, Guoqiang Shen, Xiangwen Zhang, Shi Xue Dou, et al. Efficient water oxidation through strongly coupled graphitic c 3 n 4 coated cobalt hydroxide nanowires. *Journal of Materials Chemistry A*, 4(33):12940–12946, 2016.

[13] Fang Song, Lichen Bai, Aliki Moysiadou, Seunghwa Lee, Chao Hu, Laurent Liardet, and Xile Hu. Transition metal oxides as electrocatalysts for the oxygen evolution reaction in alkaline solutions: an application-inspired renaissance. *Journal of the American Chemical Society*, 140(25):7748–7759, 2018.

[14] Bao Yu Xia, Ya Yan, Nan Li, Hao Bin Wu, Xiong Wen David Lou, and Xin Wang. A metal–organic framework-derived bifunctional oxygen electrocatalyst. *Nature energy*, 1(1):1–8, 2016.

[15] Tobias Reier, Mehtap Oezaslan, and Peter Strasser. Electrocatalytic oxygen evolution reaction (oer) on ru, ir, and pt catalysts: a comparative study of nanoparticles and bulk materials. *Acs Catalysis*, 2(8):1765–1772, 2012.

[16] Nemanja Danilovic, Ramachandran Subbaraman, Kee-Chul Chang, Seo Hyoung Chang, Yijin J Kang, Joshua Snyder, Arvydas P Paulikas, Dusan Strmcnik, Yong-Tae Kim, Deborah Myers, et al. Activity–stability trends for the oxygen evolution reaction on monometallic oxides in acidic environments. *The journal of physical chemistry letters*, 5(14):2474–2478, 2014.

[17] Sergio Trasatti. Electrocatalysis by oxides—attempt at a unifying approach. *Journal of Electroanalytical Chemistry and Interfacial Electrochemistry*, 111(1):125–131, 1980.

[18] Serhiy Cherevko, Simon Geiger, Olga Kasian, Nadiia Kulyk, Jan-Philipp Grote, Alan Savan, Buddha Ratna Shrestha, Sergiy Merzlikin, Benjamin Breitbach, Alfred Ludwig, et al. Oxygen and hydrogen evolution reactions on ru, ruo2, ir, and iro2 thin film electrodes in acidic and alkaline electrolytes: A comparative study on activity and stability. *Catalysis Today*, 262:170–180, 2016.

[19] R.+ Kötz, HJ Lewerenz, and S Stucki. Xps studies of oxygen evolution on ru and ruo2 anodes. *Journal of The Electrochemical Society*, 130(4):825, 1983.

[20] Zhi-Peng Wu, Xue Feng Lu, Shuang-Quan Zang, and Xiong Wen Lou. Non-noble-metal-based electrocatalysts toward the oxygen evolution reaction. *Advanced Functional Materials*, 30(15):1910274, 2020.

[21] Xue Feng Lu, Ye Chen, Sibo Wang, Shuyan Gao, and Xiong Wen Lou. Interfacing manganese oxide and cobalt in porous graphitic carbon polyhedrons boosts oxygen electrocatalysis for zn–air batteries. *Advanced Materials*, 31(39):1902339, 2019.

[22] Marcel Risch, Franziska Ringleb, Mike Kohlhoff, Peter Bogdanoff, Petko Chernev, Ivelina Zaharieva, and Holger Dau. Water oxidation by amorphous cobalt-based oxides: in situ tracking of redox transitions and mode of catalysis. *Energy & Environmental Science*, 8(2):661–674, 2015.

[23] Changlin Zhang, Biwei Wang, Xiaochen Shen, Jiawei Liu, Xiangkai Kong, Steven SC Chuang, Dong Yang, Angang Dong, and Zhenmeng Peng. A nitrogen-doped ordered mesoporous carbon/graphene framework as bifunctional electrocatalyst for oxygen reduction and evolution reactions. *Nano Energy*, 30:503–510, 2016.

[24] Tobias Binninger and Marie-Liesse Doublet. The ir–oooo–ir transition state and the mechanism of the oxygen evolution reaction on iro 2 (110). *Energy & Environmental Science*, 15(6):2519–2528, 2022.

[25] Yuan Ping, Giulia Galli, and William A Goddard III. Electronic structure of iro2: the role of the metal d orbitals. *The Journal of Physical Chemistry C*, 119(21):11570–11577, 2015.

[26] Daniel Weber, Leslie M Schoop, Daniel Wurmbrand, Jurgen Nuss, Elizabeth M Seibel, Fazel Fallah Tafti, Huiwen Ji, Robert J Cava, Robert E Dinnebier, and Bettina V Lotsch. Trivalent iridium oxides: layered triangular lattice iridate k0. 75na0. 25iro2 and oxyhydroxide irooh. *Chemistry of Materials*, 29(19):8338–8345, 2017.

[27] Takahiro Naito, Tatsuya Shinagawa, Takeshi Nishimoto, and Kazuhiro Takanabe. Recent advances in understanding oxygen evolution reaction mechanisms over iridium oxide. *Inorganic Chemistry Frontiers*, 8(11):2900–2917, 2021.

[28] Shuyan Gong, Taiyan Zhang, Jing Meng, Wenming Sun, and Yang Tian. Advances in the mechanism investigation for the oxygen evolution reaction: fundamental theory and monitoring techniques. *Materials Chemistry Frontiers*, 2024.

[29] Richard L Doyle and Michael EG Lyons. The oxygen evolution reaction: mechanistic concepts and catalyst design. *Photoelectrochemical Solar Fuel Production: From Basic Principles to Advanced Devices*, pages 41–104, 2016.

[30] Daniel Weber, Leslie M Schoop, Daniel Wurmbrand, Sourav Laha, Filip Podjaski, Viola Duppel, Kathrin Müller, Ulrich Starke, and Bettina V Lotsch. Irooh nanosheets as acid stable electrocatalysts for the oxygen evolution reaction. *Journal of Materials Chemistry A*, 6(43):21558–21566, 2018.

[31] D. R. Hartree. The wave mechanics of an atom with a non-coulomb central field. part i. theory and methods. *Mathematical Proceedings of the Cambridge Philosophical Society*, 24(1):89–110, Jan 1928.

[32] Richard M. Martin. *Electronic structure: Basic theory and practical methods*. Cambridge University Press, 2020.

[33] V. Fock. Näherungsmethode zur lösung des quantenmechanischen mehrkörperproblems. *Zeitschrift für Physik*, 61(1-2):126–148, 1930.

[34] L.H. Thomas. The calculation of atomic fields. *Mathematical Proceedings of the Cambridge Philosophical Society*, 23:542–548, 1927.

[35] E. Fermi. Un metodo statistico per la determinazione di alcune proprietà dell'atomo. *Rendiconti della Accademia Nazionale dei Lincei*, 6:602–607, 1927.

[36] Pierre Hohenberg and Walter Kohn. Inhomogeneous electron gas. *Physical Review*, 136(3B):B864–B871, 1964.

[37] Walter Kohn and Lu Jeu Sham. Self-consistent equations including exchange and correlation effects. *Physical Review*, 140(4A):A1133–A1138, 1965.

[38] B Joakim Nyman. Point defects and ion conduction in solid oxides: a first-principles case study of la2zr2o7. 2010.

[39] Joakim Löfgren. *Elements of modeling nanoparticle growth: Surface thermodynamics and dispersive interactions*. Chalmers Tekniska Hogskola (Sweden), 2017.

[40] Pablo Echenique and José L. Alonso. A mathematical and computational review of hartree–fock scf methods in quantum chemistry. *Molecular Physics*, 105(23-24):3057–3098, 2007.

[41] Yutaka Shikano, Hiroshi C. Watanabe, Ken M. Nakanishi, Kosuke Mitarai, and Keisuke Fujii. Post-hartree–fock method in quantum chemistry for quantum computer. *The European Physical Journal Special Topics*, 230:2405–2418, 2021.

[42] Rickard Armiento. *Density Functional Theory for Systems with Electronic Edges*. Citeseer, 2000.

[43] Wolfram Koch and Max C. Holthausen. *A Chemist's Guide to Density Functional Theory*. John Wiley & Sons, 2015.

[44] Walter Kohn and LJ Sham. Density functional theory. In *CONFERENCE PROCEEDINGS-ITALIAN PHYSICAL SOCIETY*, volume 49, pages 561–572. EDITRICE COMPOSITORI, 1996.

[45] Yusuke Nomura and Ryosuke Akashi. Density functional theory. *arXiv preprint arXiv:2210.07647*, 2022.

[46] Jorge Kohanoff. *Electronic Structure Calculations for Solids and Molecules: Theory and Computational Methods*. Cambridge University Press, 2006.

[47] Lorenz Falling. *Potential-driven surface phase transitions on iridium (hydr-) oxides and their relation to electrolytic water splitting*. PhD thesis, Technische Universität Berlin, 2020.

[48] Lev Kantorovich. *Quantum theory of the solid state: an introduction*, volume 136. Springer Science & Business Media, 2004.

[49] Zhiguo Yi. *Ab-initio Study of Semi-conductor and Metallic Systems: From Density Functional Theory to Many Body Perturbation Theory*. Osnabrück University, 2009.

[50] Supriyo Acharya. *Lithiation of Silicon Carbide*. PhD thesis, University of Stavanger, 2018.

[51] Klaus Capelle. A bird's-eye view of density-functional theory. *Brazilian Journal of Physics*, 36(4A):1318–1343, 2006.

[52] Walter Kohn. Nobel lecture: Electronic structure of matter—wave functions and density functionals. *Reviews of Modern Physics*, 71(5):1253–1266, 1999.

[53] Katharina Gelbenegger. Masterarbeit/master's thesis. Master's thesis, University of Vienna, 2018.

[54] Jorge Mario Osorio Guillén. *Density Functional Theory in Computational Materials Science*. PhD thesis, Acta Universitatis Upsaliensis, 2004.

[55] Zhiping Yin. *Microscopic mechanisms of magnetism and superconductivity studied from first principle calculations*. University of California, Davis, 2009.

[56] Hao Huang. *A density functional theory study into the mechanism and reactivity in heterogeneous system*. PhD thesis, Queen's University Belfast, 2021.

[57] John P Perdew, JA Chevary, SH Vosko, Koblar A Jackson, Mark R Pederson, DJ Singh, and Carlos Fiolhais. Erratum: Atoms, molecules, solids, and surfaces: Applications of the generalized gradient approximation for exchange and correlation. *Physical Review B*, 48(7):4978, 1993.

[58] Axel D Becke. Density-functional thermochemistry. i. the effect of the exchange-only gradient correction. *The Journal of chemical physics*, 96(3):2155–2160, 1992.

[59] EI Proynov, E Ruiz, A Vela, and DR Salahub. Determining and extending the domain of exchange and correlation functionals. *International Journal of Quantum Chemistry*, 56(S29):61–78, 1995.

[60] Bjørk Hammer, Karsten Wedel Jacobsen, and Jens Kehlet Nørskov. Role of nonlocal exchange correlation in activated adsorption. *Physical review letters*, 70(25):3971, 1993.

[61] DR Hamann. Generalized gradient theory for silica phase transitions. *Physical Review Letters*, 76(4):660, 1996.

[62] Ales Zupan, Kieron Burke, Matthias Ernzerhof, and John P Perdew. Distributions and averages of electron density parameters: Explaining the effects of gradient corrections. *The Journal of chemical physics*, 106(24):10184–10193, 1997.

[63] John P Perdew, Kieron Burke, and Matthias Ernzerhof. Generalized gradient approximation made simple. *Physical review letters*, 77(18):3865, 1996.

[64] John P Perdew, P Ziesche, and H Eschrig. Electronic structure of solids' 91, 1991.

[65] Federico Zahariev, Sarom Sok Leang, and Mark S Gordon. Functional derivatives of meta-generalized gradient approximation (meta-gga) type exchange-correlation density functionals. *The Journal of Chemical Physics*, 138(24), 2013.

[66] Axel D. Becke. Density-functional thermochemistry. iv. a new dynamical correlation functional and implications for exact-exchange mixing. *The Journal of Chemical Physics*, 104(3):1040–1046, 1996.

[67] Jianmin Tao, John P. Perdew, Viktor N. Staroverov, and Gustavo E. Scuseria. Climbing the density functional ladder: Nonempirical meta–generalized gradient approximation designed for molecules and solids. *Physical Review Letters*, 91(14):146401, 2003.

[68] Jianwei Sun, Adrienn Ruzsinszky, and John P. Perdew. Strongly constrained and appropriately normed semilocal density functional. *Physical Review Letters*, 115(3):036402, 2015.

[69] Ying Wang, Xin Jin, Hua-Wei Sun Yu, Donald G. Truhlar, and Xiao He. Revised m06-l functional for improved accuracy on chemical reaction barrier heights, noncovalent interactions, and solid-state physics. *Proceedings of the National Academy of Sciences*, 114(32):8487–8492, 2017.

[70] Max Dion, Håkan Rydberg, Elsebeth Schröder, David C. Langreth, and Bengt I. Lundqvist. Van der waals density functional for general geometries. *Physical Review Letters*, 92(24):246401, 2004.

[71] Jess Wellendorff, Keld T. Lundgaard, Karsten W. Jacobsen, and Thomas Bligaard. Density functionals for surface science: Exchange-correlation model development with bayesian error estimation. *Physical Review B*, 85(23):235149, 2012.

[72] Stefan Grimme, J. Antony, S. Ehrlich, and H. Krieg. A consistent and accurate ab initio parametrization of density functional dispersion correction (dft-d) for the 94 elements h-pu. *The Journal of Chemical Physics*, 132(15):154104, 2010.

[73] John P. Perdew, Viktor N. Staroverov, Gustavo E. Scuseria, and Gábor I. Csonka. Prescription for the design and selection of density functional approxi-

mations: More constraint satisfaction with fewer fits. *The Journal of Chemical Physics*, 123(6):062201, 2005.

[74] John P. Perdew. Accurate density functional for the energy: Real-space cutoff of the gradient expansion for the exchange hole. *Physical Review Letters*, 55(16):1665–1668, 1985.

[75] Georg Kresse and Jürgen Hafner. Ab initio molecular dynamics for liquid metals. *Physical review B*, 47(1):558, 1993.

[76] Georg Kresse and Jürgen Hafner. Ab initio molecular-dynamics simulation of the liquid-metal–amorphous-semiconductor transition in germanium. *Physical Review B*, 49(20):14251, 1994.

[77] Georg Kresse and Jürgen Furthmüller. Efficiency of ab-initio total energy calculations for metals and semiconductors using a plane-wave basis set. *Computational materials science*, 6(1):15–50, 1996.

[78] Georg Kresse and Jürgen Furthmüller. Efficient iterative schemes for ab initio total-energy calculations using a plane-wave basis set. *Physical review B*, 54(16):11169, 1996.

[79] Georg Kresse and Daniel Joubert. From ultrasoft pseudopotentials to the projector augmented-wave method. *Physical review b*, 59(3):1758, 1999.

[80] Vei Wang, Nan Xu, Jin-Cheng Liu, Gang Tang, and Wen-Tong Geng. Vaspkit: A user-friendly interface facilitating high-throughput computing and analysis using vasp code. *Computer Physics Communications*, 267:108033, 2021.

[81] Shyue Ping Ong, William Davidson Richards, Anubhav Jain, Geoffroy Hautier, Michael Kocher, Shreyas Cholia, Dan Gunter, Vincent L Chevrier, Kristin A Persson, and Gerbrand Ceder. Python materials genomics (pymatgen): A robust, open-source python library for materials analysis. *Computational Materials Science*, 68:314–319, 2013.

[82] Alex M Ganose, Adam J Jackson, and David O Scanlon. sumo: Command-line tools for plotting and analysis of periodic* ab initio* calculations. *Journal of Open Source Software*, 3(28):717, 2018.

[83] Atsushi Togo, Laurent Chaput, Terumasa Tadano, and Isao Tanaka. Implementation strategies in phonopy and phono3py. *J. Phys. Condens. Matter*, 35(35):353001, 2023.

[84] Atsushi Togo. First-principles phonon calculations with phonopy and phono3py. *J. Phys. Soc. Jpn.*, 92(1):012001, 2023.

[85] Peter E Blöchl. Projector augmented-wave method. *Physical review B*, 50(24):17953, 1994.

[86] John P. Perdew, Kieron Burke, and Matthias Ernzerhof. Generalized gradient approximation made simple. *Physical Review Letters*, 77(18):3865–3868, 1996.

[87] Oleg A Vydrov and Troy Van Voorhis. Nonlocal van der waals density functional: The simpler the better. *The Journal of chemical physics*, 133(24), 2010.

[88] Haowei Peng, Zeng-Hui Yang, John P Perdew, and Jianwei Sun. Versatile van der waals density functional based on a meta-generalized gradient approximation. *Physical Review X*, 6(4):041005, 2016.

[89] Haowei Peng and John P Perdew. Rehabilitation of the perdew-burke-ernzerhof generalized gradient approximation for layered materials. *Physical Review B*, 95(8):081105, 2017.

[90] Qian Dang, Haiping Lin, Zhenglong Fan, Lu Ma, Qi Shao, Yujin Ji, Fangfang Zheng, Shize Geng, Shi-Ze Yang, Ningning Kong, et al. Iridium metallene oxide for acidic oxygen evolution catalysis. *Nature Communications*, 12(1):6007, 2021.

DEPARTMENT OF PHYSICS
CHALMERS UNIVERSITY OF TECHNOLOGY
Gothenburg, Sweden
www.chalmers.se

CHALMERS
UNIVERSITY OF TECHNOLOGY